Three-dimensional analytical model for the pull-out response of anchor-mortar-concrete anchorage system based on interfacial bond failure

Yan-Jie Wang[a], Zhi-Min Wu[a*], Jian-Jun Zheng[b], Xiang-Ming Zhou[c]

[a]State Key Laboratory of Coastal and Offshore Engineering, Dalian University of Technology, Dalian 116024, China.

[b]School of Civil Engineering and Architecture, Zhejiang University of Technology, Hangzhou 310023, China.

[c]Department of Civil & Environmental Engineering, Brunel University London, Uxbridge UB8 3PH, UK.

ABSTRACT

The interfacial bond behavior plays a significant role in determining the load transfer performance of anchor systems. Numerous analytical models have been proposed to investigate the pull-out behavior of grouted anchors, but no closed-form three-dimensional solution has been derived for the pull-out response of anchor systems with respect to interfacial bond failure. By considering the bond failure at the anchor-mortar interface, this paper presents a three-dimensional analytical model for predicting the pull-out response of grouted anchors based on a tri-linear bond-slip model. Specifically, the closed-form expressions are derived for the axial displacement, axial stress, and shear stress of the anchor

*Corresponding author.

E-mail address: wuzhimin@dlut.edu.cn (Z.M. Wu).

and concrete, the load-displacement relationship of the anchor, and the interfacial shear stress at various possible pull-out stages. Furthermore, the load-displacement relationships and interfacial shear stress distributions are analyzed for different bond lengths during the whole pull-out process. The validity of the three-dimensional model is verified with experimental results collected from the literature. Through a systematic parametric study, the effect of bond length on the ultimate load and load-displacement response is investigated with the proposed model. It is shown that the ultimate load increases with the increase of bond length significantly before a critical bond length is reached but thereafter at a smaller and steady rate. Moreover, a longer bond length improves the ductility of the anchorage and the snapback phenomenon in the load-displacement response is dependent on the bond length, while the intensity of snapback increases with an increase in bond length. The proposed model is capable of better understanding the debonding mechanism and can be employed by engineers and researchers to predict the ultimate load capacity and load-displacement response of anchor systems.

Keywords: Anchor system; Interfacial shear stress distribution; Ultimate load; Load-displacement relationship; Analytical solution.

Nomenclature

$A_{1\text{-}9}$, $B_{1\text{-}9}$, $C_{1\text{-}9}$, $D_{1\text{-}9}$	coefficients	w_c	axial displacement of concrete
a	radius of anchor	w_m	axial displacement of mortar
b	inner radius of concrete	w_s	axial displacement of anchor
E_c	Young's modulus of concrete	Δ	axial displacement at loading point
E_s	Young's modulus of anchor	δ	slip at anchor-mortar interface
G	shear modulus of mortar	δ_0	slip at the free end
G_c	shear modulus of concrete	δ_1	slip at anchor-mortar interface corresponding to τ_u
G_s	shear modulus of anchor		
h	outer radius of concrete	δ_2	slip at anchor-mortar interface corresponding to τ_r
L	bond length		
L_{cri}	critical bond length	δ_3	a hypothetical slip which is much larger than δ_2
L_e	elastic length		
L_f	frictional length	δ_L	slip at the loaded end
L_s	softening length	μ_c	Poisson's ratio of concrete
L_{sc}	critical softening length	μ_s	Poisson's ratio of anchor
L_{sn}	minimum bond length that exhibits snapback	σ_c	axial stress of concrete
		σ_s	axial stress of anchor
L_u	minimum bond length for elastic-softening-frictional stage to appear	τ	shear stress at anchor-mortar interface
		τ_c	shear stress of concrete
P	pull-out load	τ_m	shear stress of mortar
P_e	elastic ultimate load	τ_r	frictional strength
P_{emax}	ultimate load obtained by experiments	τ_s	shear stress of anchor
		τ_u	shear strength
P_{max}	ultimate load	λ, φ, β, ζ	eigenvalues

1. Introduction

Anchor systems have been widely applied in practical engineering, such as building retrofitting, slope strengthening, anti-floating engineering, tunnel supporting and mining [1-4]. In the past several decades, much research has been conducted to predict the potential failure modes of anchor systems [5-8]. It was found that the failure of an anchor system may occur in the anchor, in the concrete, at the anchor-mortar or mortar-concrete interface, or in a combined modes. However, numerous studies have found that the bond failure at the anchor-mortar interface is more common [9-12]. With reference to this failure mode, Cook [5] proposed a uniform bond stress model by assuming a constant shear stress along the bond length. However, this assumption is only valid for a short bond length since the shear stress distribution along the bond length becomes more non-uniform with the increase of bond length. Therefore, the determination of the accurate shear stress distribution at the anchor-mortar interface is crucial for predicting the ultimate load capacity of grouted anchors.

With regard to field and laboratory pull-out tests, considerable investigations have been undertaken on the effects of geometric and material parameters on the interfacial bond behavior of grouted anchors [9, 13-20]. Moreover, various bond-slip models have been proposed to study the interfacial behavior of grouted anchors. Based on experimental results, Benmokrane et al. [9] presented a tri-linear bond-slip model to describe the bond behavior of the anchor-mortar interface. Ma et al. [21] proposed a non-linear bond-slip model to characterize the bolt-grout interface, which is in good agreement with the results of pull-out tests. By taking into account the unloading effect, Zheng and Dai [22] introduced a slightly simplified bond-slip model of the bar-grout interface to study the pull-out response of FRP anchors using a numerical method.

Extensive analytical studies on the full-range pull-out behavior of grouted anchors have also been carried out and reported in the literature. An analytical method was proposed by Yang et al. [23] for analyzing the pull-out behavior of grouted anchors due to interfacial debonding under two boundary conditions. It was found that the interfacial debonding crack may occur at the loading end, the free end or both of them, depending on the axial stiffnesses of the anchor and concrete. Furthermore, a series of analytical studies were conducted to predict the ultimate pull-out capacity of grouted anchors due to the shear failure of mortar

[24], the cone failure of concrete, and interfacial debonding [25]. For FRP anchors embedded in steel tubes with cement grout, Wu et al. [26] presented a theoretical model to predict the maximum pull-out load of FRP anchors based on a tri-linear bond slip model. Zheng and Dai [27] derived a closed-form analytical solution to predict the pull-out response of FRP ground anchors for linear elastic, softening, and frictional zones. Using a tri-linear bond-slip model, Ren et al. [28] derived an analytical solution to study the mechanical behavior and debonding process of grouted rockbolts at different loading stages. To investigate the load transfer mechanism of grouted cable bolts, an analytical study was conducted by Chen et al. [29], in which the interfacial shear stress distribution along the bond length during the entire pull-out process was analyzed. Based on a tri-linear bond-slip model, Ma et al. [30] provided an analytical model for rockbolts using the slip-strain relationship of rockbolts and considering the pre- and post-yielding behavior of the bolt material. By taking into consideration the end effect of embedded anchors, Saleem and Tsubaki [31, 32] and Saleem [33] proposed a shear-lag analytical model and developed a new type of two-layer anchor-infill assembly that can be employed to evaluate the pull-out load-displacement response of post-installed anchors under monotonic and cyclic loading. Saleem and Nasir [34] presented an analytical model to evaluate the bond performance at the steel-concrete interface and to predict the pull-out response of steel anchor bolts subjected to impact loading. More recently, Saleem [35] presented a new analytical model that can be employed to simulate the load-displacement response of steel bolts subjected to cyclic pull-out push-in loading. In the model, the effect of concrete crushing was incorporated. Further, when the multiple possibilities related to crack propagation were considered, a multiple crack extension model was presented by Saleem [36]

for predicting the pull-out response of anchor bolts subjected to impact loading. Huang et al. [37] proposed a one-dimensional closed-form solution. With the solution, the load capacity and deformation response at any pull-out stage of grouted anchors could be evaluated using a tri-linear bond-slip model. By taking into account the temperature effect, Lahoual et al. [38] presented a nonlinear shear-lag analytical model for the pull-out behavior of chemical anchors, which allows for predicting the stress field and fire resistance duration when any temperature distribution is applied.

Moreover, current theoretical studies for debonding of FRP plates from the concrete substrate can provide some references on the bond behavior between the anchor and mortar. Recently, based on a bilinear bond-slip model, Caggiano et al. [39] proposed a closed-form analytical solution for describing the full-range load-slip behavior of FRP plates bonded to a brittle substrate, in which the whole interfacial debonding processes for long and short bond lengths were presented in detail. Based on the pioneer work by Caggiano et al. [39], Vaculik et al. [40] presented a full-range analytical solution using the bilinear bond-slip model, which allows for residual friction used for simulating the load-displacement response at various stages during the evolution of debonding.

Although numerous studies on the mechanical behavior of grouted anchors have been carried out, analytical studies in three dimensions are relatively few in the literature. Prieto-Muñoz et al. [41] presented an axisymmetric solution for the anchor and the adhesive layer based on an elastic analysis, in which the embedded end of the anchor was regarded to be bonded or debonded. Furthermore, a viscoelastic analytical model was developed by Prieto-Muñoz et al. [42] to predict the creep behavior of anchor systems. Upadhaya and Kumar [43] proposed an axisymmetric model to predict the pull-out capacity and stress field of adhesive anchors with the eigenfunction expansion method, which was found to be in good agreement with the finite element method and experimental results.

Despite significant research efforts on the pull-out behavior of grouted anchors, the load transfer performance and interfacial bond failure process of grouted anchors have not been fully understood. (1) In most of the aforementioned analytical work [21-40], a simple one-dimensional model was employed, in which the effect of Poisson's ratio of each phase in anchor systems is not taken into consideration. However, due to the axisymmetric nature of anchorages, the study on the pull-out response of anchors is, in essence, a three-dimensional axisymmetric problem [41]. Thus, a three-dimensional axisymmetric model is needed to provide a more complete and precise prediction on the load capacity and stress field of anchor systems during the whole pull-out process for the purpose of design. (2) In the previous three-dimensional axisymmetric analytical models [41-43], the bond between the anchor and adhesive is considered to be perfect and the materials in the anchor system are assumed to be either elastic (anchor), elastic or viscoelastic (adhesive), or rigid (concrete). In these studies, stress based failure criteria are employed to estimate the ultimate load capacity. However, the postpeak stress and displacement fields are not considered. Moreover, the full-range pull-out load-displacement response is not taken into account in these analyses. It is seen from the previous studies that the nonlinear pull-out behavior of anchors is particularly important for the design of anchor systems and the interfacial debonding process has a significant effect on the pull out behavior [27-29, 37]. Furthermore, the deformation of the concrete substrate plays a pivotal role in the pull-out capacity and load-displacement response of grouted anchors [2, 15, 16, 19, 20, 23-25]. However, to the best of our knowledge, a full-range closed-form three-dimensional axisymmetric solution for the nonlinear pull-out response of grouted anchors has not been reported so far.

The purpose of this paper is to develop a three-dimensional analytical model, in which a tri-linear bond-slip model representing the bond behavior of the anchor-mortar interface is employed to predict the full-range failure process and pull-out response of grouted anchors. Afterwards, the analytical model is validated with laboratory pull-out test results and the effect of bond length on the ultimate load and load-displacement curves is discussed.

2. Fundamental assumptions and governing equations

A typical anchor system is schematically shown in Fig. 1, where the anchor is embedded in concrete. L, a, b, and h are the bond length, the anchor radius, the inner and outer radii of the concrete, respectively. E_s, G_s, μ_s, E_c, G_c, and μ_c denote Young's modulus, the shear modulus, and Poisson's ratio of the anchor and concrete, respectively. As shown in Fig. 1, the embedded end of the anchor system at $z = 0$ remains completely free, while the outer boundary of concrete at $r = h$ is fixed. In the present study, the following assumptions are introduced.

(1) The anchor, mortar, and concrete are treated as elastic materials. Mortar with shear modulus G is only subjected to shear.

(2) The crack occurs only at the anchor-mortar interface, initiates at the loaded end, and propagates towards the free end of the anchorage until complete debonding.

(3) The bending effect of concrete is neglected and the radial deformations of the anchor and

concrete are assumed to be zero.

(4) The end effect of the embedded anchor is not considered.

A traditional tri-linear bond-slip model representing the bond behavior of the anchor-mortar interface has been widely used in several studies [9, 21, 26-30, 37], as depicted in Fig. 2(a). In the frictional zone of the model, the interfacial shear stress remains constant [9]. However, it should be noted that in the present work, due to the limitation of interfacial boundary conditions, the solutions for the stress and displacement fields in the frictional zone cannot be derived when the interfacial shear stress remains constant. Therefore, a slip δ_3 is assumed in the present study, as shown in Fig. 2(b). When the value of δ_3 is far greater than that of δ_2, the interfacial shear stress in the frictional zone can be regarded as constant. For this purpose, δ_3 is taken as 100 times δ_2 so that the bond-slip model shown in Fig. 2(b) can approximately represent the traditional tri-linear bond-slip model shown in Fig. 2(a).

The tri-linear bond-slip model shown in Fig. 2(b) consists of three branches: (1) the first branch (linearly ascending to (δ_1, τ_u)) represents the elastic behavior of the interface; (2) the second branch (linearly descending to (δ_2, τ_r)) characterizes the softening behavior of the interface; and (3) the third branch (linear descending to ($\delta_3, 0$)) corresponds to the frictional component. The shear stress at the anchor-mortar interface τ can be mathematically expressed in terms of the shear slip δ as

$$\tau = \begin{cases} \dfrac{\tau_u}{\delta_1}\delta & \text{for } 0 \le \delta \le \delta_1 \\ -\dfrac{\tau_u - \tau_r}{\delta_2 - \delta_1}\delta + \dfrac{\tau_u\delta_2 - \tau_r\delta_1}{\delta_2 - \delta_1} & \text{for } \delta_1 \le \delta \le \delta_2 \\ -\dfrac{\tau_r}{\delta_3 - \delta_2}\delta + \dfrac{\tau_r\delta_3}{\delta_3 - \delta_2} & \text{for } \delta_2 \le \delta \le \delta_3 \end{cases} \tag{1}$$

where τ_u and τ_r denote the bond and frictional strengths at the anchor-mortar interface and δ_1

and δ_2 are the relative shear slips corresponding to τ_u and τ_r, respectively.

According to assumption (1), the mortar is only subjected to pure shear. For a cylindrical mortar element shown in Fig. 3, the equilibrium of shear forces in the *z* direction yields [1]

$$\frac{1}{\tau_m}\mathrm{d}\tau_m = -\frac{1}{r}\mathrm{d}r \tag{2}$$

where τ_m is the shear stress in mortar at distance *r* from the *z* axis. Integrating Eq. (2) gives

$$\tau_m = \frac{a}{r}\tau \tag{3}$$

From assumption (3), all deformations are confined to the axial direction and the displacement of mortar in the radial direction is zero. According to Hook's law in shear, the shear stress in the grout τ_m can be expressed in terms of the axial displacement of the grout $w_m(r)$ as

$$\tau_m = -G\frac{\mathrm{d}w_m(r)}{\mathrm{d}r} \tag{4}$$

Substituting Eq. (3) into Eq. (4) gives

$$\mathrm{d}w_m(r) = -\frac{a\tau}{G}\cdot\frac{\mathrm{d}r}{r} \tag{5}$$

Integrating Eq. (5) with respect to r from a to b yields

$$w_m(r=b) - w_m(r=a) = -\frac{a\tau}{G}\ln\frac{b}{a} \tag{6}$$

From assumption (2), the mortar-concrete interface is considered to be fully bonded and the displacements of mortar and concrete are the same at the mortar-concrete interface. Thus, it follows from Eq. (6) that the shear slip at the anchor-mortar interface δ can be expressed as

$$\delta = w_s(r=a) - w_m(r=a) = w_s(r=a) - w_c(r=b) - \frac{a\tau}{G}\ln\frac{b}{a} \tag{7}$$

where w_s and w_c denote the axial displacements of the anchor and concrete, respectively.

From the continuity conditions at the anchor-mortar and mortar-concrete interfaces, the shear stress in concrete at the mortar-concrete interface $\tau_c\left(r=b\right)$ can be expressed as

$$\tau_c\left(r=b\right)=-\frac{a}{b}\tau=\frac{a}{b}\tau_s\left(r=a\right) \tag{8}$$

where τ_s is the shear stress in the anchor. Substituting Eq. (7) into Eq. (1) yields

$$\tau=\begin{cases}K\left[w_s\left(r=a,z\right)-w_c\left(r=b,z\right)\right] & \text{for elastic zone}\\ -K_1\left[w_s\left(r=a,z\right)-w_c\left(r=b,z\right)-K_2\right] & \text{for softening zone}\\ -K_3\left[w_s\left(r=a,z\right)-w_c\left(r=b,z\right)-\delta_3\right] & \text{for frictional zone}\end{cases} \tag{9}$$

where

$$K=\frac{1}{\dfrac{\delta_1}{\tau_u}+\dfrac{a}{G}\ln\dfrac{b}{a}};\quad K_1=\frac{1}{\dfrac{\delta_2-\delta_1}{\tau_u-\tau_r}-\dfrac{a}{G}\ln\dfrac{b}{a}};\quad K_2=\frac{\delta_2\tau_u-\delta_1\tau_r}{\tau_u-\tau_r};\quad K_3=\frac{1}{\dfrac{\delta_3-\delta_2}{\tau_r}-\dfrac{a}{G}\ln\dfrac{b}{a}} \tag{10}$$

Based on the strain-displacement relationships for axisymmetric problems and assumption (3), the constitutive law in the axial direction can be used to describe the respective relationships between the axial displacement w_i, the axial stress σ_i, and the shear stress τ_i

$$\sigma_i=\frac{E_i\left(1-\mu_i\right)}{\left(1+\mu_i\right)\left(1-2\mu_i\right)}\frac{\partial w_i}{\partial z};\quad \tau_i=\frac{E_i}{2\left(1+\mu_i\right)}\frac{\partial w_i}{\partial r} \tag{11}$$

With Eq. (11), the governing equation for the anchor and concrete can be expressed as

$$\frac{2(1-\mu_i)}{1-2\mu_i}\frac{\partial^2 w_i}{\partial z^2}+\frac{\partial^2 w_i}{\partial r^2}+\frac{1}{r}\frac{\partial w_i}{\partial r}=0 \tag{12}$$

where i is equal to s for the anchor and c for concrete.

3. Analytical solutions

The various possible pull-out cases during the propagation process of debonding are shown in Fig. 4, where δ_0 and δ_L are the slips at the free end and loaded end, respectively. It is noted that the value of L_u will be defined later by Eq. (60). The failure process under the pull-out load P may exhibit elastic, elastic-softening, elastic-softening-frictional, softening-frictional, and frictional for a long bond length [27, 28]. However, when the bond length L is not long enough, the softening stage rather than the elastic-softening-frictional stage may occur [29, 37, 40]. In the current study, the analytical solutions for the displacement and stress fields of the anchor system under the two scenarios are derived by solving the governing Eq. (12) with boundary conditions.

3.1. Elastic stage

Under a small pull-out load, there is no softening or friction along the anchor-mortar interface. In this case, the interface behaves elastic. Based on separation of variables, the general solutions of Eq. (12) for the elastic stage can be expressed as

$$w_s\left(r,z\right)=\left[A\sinh\left(\lambda z\right)+B\cosh\left(\lambda z\right)\right]J_0\left(d_s r\right) \tag{13}$$

$$w_c\left(r,z\right)=\left[C\sinh\left(\lambda z\right)+D\cosh\left(\lambda z\right)\right]\left[Y_0\left(d_c r\right)J_0\left(d_c h\right)-J_0\left(d_c r\right)Y_0\left(d_c h\right)\right] \tag{14}$$

where A, B, C, D, λ, d_s, and d_c are coefficients to be determined with the boundary conditions. Based on the assumption that the outer boundary of concrete is fixed, the displacement of concrete can be simplified to Eq. (14) by satisfying $w_c\left(r=h,z\right)=0$. Substitution of Eqs. (13) and (14) into Eq. (11) yields

$$\sigma_s\left(r,z\right)=E_1\lambda J_0\left(d_s r\right)\left[A\cosh\left(\lambda z\right)+B\sinh\left(\lambda z\right)\right] \tag{15}$$

$$\tau_s\left(r,z\right)=-d_s G_s\left[A\sinh\left(\lambda z\right)+B\cosh\left(\lambda z\right)\right]J_1\left(d_s r\right) \tag{16}$$

$$\sigma_c\left(r,z\right)=E_2\lambda\left[C\cosh\left(\lambda z\right)+D\sinh\left(\lambda z\right)\right]\left[Y_0\left(d_c r\right)J_0\left(d_c h\right)-J_0\left(d_c r\right)Y_0\left(d_c h\right)\right] \tag{17}$$

$$\tau_c\left(r,z\right)=-d_c G_c\left[C\sinh\left(\lambda z\right)+D\cosh\left(\lambda z\right)\right]\left[Y_1\left(d_c r\right)J_0\left(d_c h\right)-J_1\left(d_c r\right)Y_0\left(d_c h\right)\right] \tag{18}$$

where

$$d_i=\sqrt{\frac{2(1-\mu_i)}{1-2\mu_i}}\lambda\,;\quad E_1=\frac{E_s(1-\mu_s)}{(1+\mu_s)(1-2\mu_s)}\,;\quad E_2=\frac{E_c(1-\mu_c)}{(1+\mu_c)(1-2\mu_c)} \tag{19}$$

The boundary conditions are as follows

$$\sigma_s(z=0,r)=0\,;\quad \sigma_c(z=0,r)=0\,;\quad \int_0^a 2\pi r\cdot\sigma_s(z=L,r)\mathrm{d}r=P \tag{20}$$

$$\frac{b}{a}\tau_c(r=b,z)=\tau_s(r=a,z)=-\tau(z)=-K\left[w_s(r=a,z)-w_c(r=b,z)\right] \tag{21}$$

With these boundary conditions, the following coefficients are obtained as

$$A=C=0\,;\quad B=\frac{P\lambda}{2\pi a\sinh(\lambda L)d_sG_sJ_1(d_sa)}\,;\quad D=N_1B\,;\ \text{and} \tag{22}$$

$$N_1=\frac{ad_sG_sJ_1(d_sa)}{bd_cG_c\left[Y_1(d_cb)J_0(d_ch)-J_1(d_cb)Y_0(d_ch)\right]} \tag{23}$$

The coefficient λ can be solved by combining Eqs. (13), (14), (16), (18), and (21) as

$$d_sG_sJ_1(d_sa)=K\left\{J_0(d_sa)-N_1\left[Y_0(d_cb)J_0(d_ch)-J_0(d_cb)Y_0(d_ch)\right]\right\} \tag{24}$$

From Eq. (24), a series of roots can be obtained. For simplicity, only the first root is used in the elastic stage [41, 42]. With λ determined, the value of d_i can be obtained from Eq. (19). The shear stress τ can be obtained from the condition (21) as

$$\tau(z)=\frac{P\lambda\cosh(\lambda z)}{2\pi a\sinh(\lambda L)} \tag{25}$$

If the displacement of the anchor at the loading point denotes Δ, the load-displacement relationship can be obtained by substituting $r=0$ and $z=L$ into Eq. (13) as

$$P=\frac{2\pi ad_sG_sJ_1(d_sa)\Delta}{\lambda}\tanh(\lambda L) \tag{26}$$

As the load P increases, this stage ends when the shear stress τ at the loaded end reaches τ_u. Substituting $\tau(z=L)=\tau_u$ into Eq. (25) gives the elastic ultimate load P_e

$$P_e=\frac{2\pi a\tau_u}{\lambda}\tanh(\lambda L) \tag{27}$$

It is noted that P_e represents the pull-out load before the interface starts softening.

3.2. Elastic-softening stage

In this stage, softening first appears at the loaded end and the peak shear stress moves towards the free end. Thus, the whole anchor-mortar interface consists of an elastic zone of length L_e and a softening zone of length L_s. With the boundary and continuous conditions in this stage, the general solutions of Eq. (12) for the elastic zone can be written as

$$w_s(r,z) = \left[A_1 \sinh(\lambda z) + B_1 \cosh(\lambda z)\right] J_0(d_s r) + \left[A_2 \sinh(\varphi z) + B_2 \cosh(\varphi z)\right] J_0(d_{\varphi s} r) \quad (28)$$

$$\begin{aligned} w_c(r,z) = &\left[C_1 \sinh(\lambda z) + D_1 \cosh(\lambda z)\right]\left[Y_0(d_c r) J_0(d_c h) - J_0(d_c r) Y_0(d_c h)\right] \\ &+ \left[C_2 \sinh(\varphi z) + D_2 \cosh(\varphi z)\right]\left[Y_0(d_{\varphi c} r) J_0(d_{\varphi c} h) - J_0(d_{\varphi c} r) Y_0(d_{\varphi c} h)\right] \end{aligned} \quad (29)$$

where A_1, B_1, C_1, D_1, A_2, B_2, C_2, D_2, φ, $d_{\varphi s}$, and $d_{\varphi c}$ are unknown coefficients and

$$d_{\varphi i} = \sqrt{\frac{2(1-\mu_i)}{1-2\mu_i}}\varphi \quad (30)$$

Substituting Eqs. (28) and (29) into Eq. (11) gives

$$\begin{aligned} \sigma_s(r,z) = &E_1 \lambda J_0(d_s r)\left[A_1 \cosh(\lambda z) + B_1 \sinh(\lambda z)\right] \\ &+ E_1 \varphi J_0(d_{\varphi s} r)\left[A_2 \cosh(\varphi z) + B_2 \sinh(\varphi z)\right] \end{aligned} \quad (31)$$

$$\begin{aligned} \tau_s(r,z) = &-d_s G_s \left[A_1 \sinh(\lambda z) + B_1 \cosh(\lambda z)\right] J_1(d_s r) \\ &- d_{\varphi s} G_s \left[A_2 \sinh(\varphi z) + B_2 \cosh(\varphi z)\right] J_1(d_{\varphi s} r) \end{aligned} \quad (32)$$

$$\begin{aligned} \sigma_c(r,z) = &E_2 \lambda \left[C_1 \cosh(\lambda z) + D_1 \sinh(\lambda z)\right]\left[Y_0(d_c r) J_0(d_c h) - J_0(d_c r) Y_0(d_c h)\right] \\ &+ E_2 \varphi \left[C_2 \cosh(\varphi z) + D_2 \sinh(\varphi z)\right]\left[Y_0(d_{\varphi c} r) J_0(d_{\varphi c} h) - J_0(d_{\varphi c} r) Y_0(d_{\varphi c} h)\right] \end{aligned} \quad (33)$$

$$\begin{aligned} \tau_c(r,z) = &-d_c G_c \left[C_1 \sinh(\lambda z) + D_1 \cosh(\lambda z)\right]\left[Y_1(d_c r) J_0(d_c h) - J_1(d_c r) Y_0(d_c h)\right] \\ &- d_{\varphi c} G_c \left[C_2 \sinh(\varphi z) + D_2 \cosh(\varphi z)\right]\left[Y_1(d_{\varphi c} r) J_0(d_{\varphi c} h) - J_1(d_{\varphi c} r) Y_0(d_{\varphi c} h)\right] \end{aligned} \quad (34)$$

The boundary conditions in the elastic zone $[0, L_e]$ are as follows

$$\sigma_s(z=0,r) = 0; \quad \sigma_c(z=0,r) = 0; \quad -\tau_s(r=a, z=L_e) = \tau_u \quad (35)$$

$$\frac{b}{a}\tau_c(r=b,z) = \tau_s(r=a,z) = -\tau(z) = -K\left[w_s(r=a,z) - w_c(r=b,z)\right] \quad (36)$$

It can be seen from the conditions (21) and (36) that φ is in fact another root of Eq. (24). Based on the superposition principle and separation of variables, the general solutions of Eq. (12) for the softening zone can be expressed as

$$w_s(r,z)=\left[A_3\sin(\beta z)+B_3\cos(\beta z)\right]I_0\left(d^s r\right)+K_2 \tag{37}$$

$$w_c(r,z)=\left[C_3\sin(\beta z)+D_3\cos(\beta z)\right]\left[K_0\left(d^c r\right)I_0\left(d^c h\right)-I_0\left(d^c r\right)K_0\left(d^c h\right)\right] \tag{38}$$

$$\sigma_s(r,z)=E_1\beta I_0\left(d^s r\right)\left[A_3\cos(\beta z)-B_3\sin(\beta z)\right] \tag{39}$$

$$\tau_s(r,z)=d^s G_s\left[A_3\sin(\beta z)+B_3\cos(\beta z)\right]I_1\left(d^s r\right) \tag{40}$$

$$\sigma_c(r,z)=E_2\beta\left[C_3\cos(\beta z)-D_3\sin(\beta z)\right]\left[K_0\left(d^c r\right)I_0\left(d^c h\right)-I_0\left(d^c r\right)K_0\left(d^c h\right)\right] \tag{41}$$

$$\tau_c(r,z)=-d^c G_c\left[C_3\sin(\beta z)+D_3\cos(\beta z)\right]\left[K_1\left(d^c b\right)I_0\left(d^c h\right)+I_1\left(d^c b\right)K_0\left(d^c h\right)\right] \tag{42}$$

where A_3, B_3, C_3, D_3, β, d^s, and d^c are unknown coefficients and

$$d^i=\sqrt{\frac{2(1-\mu_i)}{1-2\mu_i}}\beta \tag{43}$$

The continuous and boundary conditions in the softening zone in $[0, L_s]$ are as follows

$$\sigma_s(z=0) \text{ and } w_s(z=0) \text{ are continuous; } -\tau_s(r=a,z=0)=\tau_u \tag{44}$$

$$\int_0^a 2\pi r\cdot\sigma_s(z=L_s,r)\mathrm{dr}=P \tag{45}$$

$$\frac{b}{a}\tau_c(r=b,z)=\tau_s(r=a,z)=-\tau(z)=K_1\left[w_s(r=a,z)-w_c(r=b,z)-K_2\right] \tag{46}$$

With the conditions (35), (36), (44), (45), and (46), the unknown coefficients A_1, B_1, C_1, D_1, A_2, B_2, C_2, D_2, A_3, B_3, C_3, and D_3 can be obtained as

$$B_1=\frac{N_2}{\cosh(\lambda L_e)};\quad B_2=\frac{N_3}{\cosh(\varphi L_e)} \tag{47}$$

$$A_1=A_2=C_1=C_2=0;\quad D_1=N_1B_1;\quad D_2=N_4B_2 \tag{48}$$

$$A_3=\frac{\beta}{d^s I_1\left(d^s a\right)}\left[\frac{N_2 d_s J_1\left(d_s a\right)\tanh(\lambda L_e)}{\lambda}+\frac{N_3 d_{\varphi s} J_1\left(d_{\varphi s} a\right)\tanh(\varphi L_e)}{\varphi}\right] \tag{49}$$

$$B_3 = -\frac{\tau_u}{d^s G_s I_1\left(d^s a\right)};\quad C_3 = N_5 A_3;\quad D_3 = N_5 B_3 \tag{50}$$

where

$$N_2 = \frac{K_2 - \dfrac{\tau_u}{d^s G_s I_1\left(d^s a\right)} - \dfrac{\tau_u}{d_{\varphi s} G_s J_1\left(d_{\varphi s} a\right)}}{1 - \dfrac{d_s J_1\left(d_s a\right)}{d_{\varphi s} J_1\left(d_{\varphi s} a\right)}};\quad N_3 = K_2 - N_2 - \frac{\tau_u}{d^s G_s I_1\left(d^s a\right)} \tag{51}$$

$$N_4 = \frac{a d_{\varphi s} G_s J_1\left(d_{\varphi s} a\right)}{b d_{\varphi c} G_c\left[Y_1\left(d_{\varphi c} b\right) J_0\left(d_{\varphi c} h\right) - J_1\left(d_{\varphi c} b\right) Y_0\left(d_{\varphi c} h\right)\right]} \tag{52}$$

$$N_5 = -\frac{a d^s G_s I_1\left(d^s a\right)}{b d^c G_c\left[K_1\left(d^c b\right) I_0\left(d^c h\right) + I_1\left(d^c b\right) K_0\left(d^c h\right)\right]} \tag{53}$$

Substituting Eqs. (37), (38), (40), and (42) into the condition (46), the remaining unknown coefficient β can be obtained by solving the following equation

$$d^s G_s I_1\left(d^s a\right) - K_1\left\{I_0\left(d^s a\right) - N_5\left[K_0\left(d^c b\right) I_0\left(d^c h\right) - I_0\left(d^c b\right) K_0\left(d^c h\right)\right]\right\} = 0 \tag{54}$$

It is noted that only one root can be obtained from Eq. (54) as the modified Bessel function is a non-oscillating function. According to Eqs. (32), (36), (40), and (46), the shear stress τ in the elastic-softening stage can be expressed as

$$\begin{aligned}\tau(z) = {} & d_s G_s B_1 \cosh(\lambda z) J_1\left(d_s a\right) \\ & + d_{\varphi s} G_s B_2 \cosh(\varphi z) J_1\left(d_{\varphi s} a\right)\end{aligned} \quad \text{in the elastic zone } [0, L_e] \tag{55}$$

$$\tau(z) = -d^s G_s\left[A_3 \sin(\beta z) + B_3 \cos(\beta z)\right] I_1\left(d^s a\right) \quad \text{in the softening zone } [0, L_s] \tag{56}$$

Substituting the condition (45) into Eq. (39) yields the pull-out load P

$$P = \frac{2\pi a d^s G_s I_1\left(d^s a\right)}{\beta}\left[A_3 \cos\left(\beta L_s\right) - B_3 \sin\left(\beta L_s\right)\right] \tag{57}$$

The displacement at the loading point Δ is obtained from Eq. (37) as

$$\Delta = A_3 \sin\left(\beta L_s\right) + B_3 \cos\left(\beta L_s\right) + K_2 \tag{58}$$

Thus, the critical softening length L_{sc} can be obtained by solving $\mathrm{d}P/\mathrm{d}L_s = 0$. If the ultimate load P_{max} occurs in this stage, it can be obtained by substituting L_{sc} into Eq. (58). As a matter of fact, as the softening zone propagates, two scenarios may occur. On one hand, the elastic-softening-frictional stage occurs when τ at the loaded end reduces to τ_r. Thus, L_s can be obtained by substituting $\tau\left(z=L_s\right)=\tau_r$ into Eq. (56) as

$$d^s G_s\left[A_3\sin\left(\beta L_s\right)+B_3\cos\left(\beta L_s\right)\right]I_1\left(d^s a\right)=-\tau_r \tag{59}$$

On the other hand, the softening stage occurs when L_s extends to L and τ at the loaded end is still greater than τ_r. At the critical situation, softening appears at the free end and friction begins at the loaded end. Substituting $L_s=L$ into Eq. (59) yields

$$L_u=L=\frac{1}{\beta}\arccos\left(\frac{\tau_r}{\tau_u}\right) \tag{60}$$

where L_u represents the minimum bond length for the elastic-softening-frictional stage to appear. It is easily shown that when the bond length is greater than L_u, the elastic-softening-frictional stage occurs. Otherwise, the softening stage will appear.

3.3. Elastic-softening-frictional stage

At this stage, frictional zone appears and extends along the interface. If the length of the frictional zone is L_f, the solutions in the elastic-softening stage, i.e., Eqs. (28) to (34), (37) to (43), and (47) to (56) are still valid by replacing L with $L-L_f$.

The general solutions of Eq. (12) for the frictional zone can be expressed as

$$w_s\left(r,z\right)=\left[A_4\sin\left(\zeta z\right)+B_4\cos\left(\zeta z\right)\right]I_0\left(d^{\zeta s}r\right)+\delta_3 \tag{61}$$

$$w_c\left(r,z\right)=\left[C_4\sin\left(\zeta z\right)+D_4\cos\left(\zeta z\right)\right]\left[K_0\left(d^{\zeta c}r\right)I_0\left(d^{\zeta c}h\right)-I_0\left(d^{\zeta c}r\right)K_0\left(d^{\zeta c}h\right)\right] \tag{62}$$

$$\sigma_s\left(r,z\right)=E_1\zeta I_0\left(d^{\zeta s}r\right)\left[A_4\cos\left(\zeta z\right)-B_4\sin\left(\zeta z\right)\right] \tag{63}$$

$$\tau_s\left(r,z\right)=d^{\zeta s}G_s\left[A_4\sin\left(\zeta z\right)+B_4\cos\left(\zeta z\right)\right]I_1\left(d^{\zeta s}r\right) \tag{64}$$

$$\sigma_c\left(r,z\right)=E_2\zeta\left[C_4\cos\left(\zeta z\right)-D_4\sin\left(\zeta z\right)\right]\left[K_0\left(d^{\zeta c}r\right)I_0\left(d^{\zeta c}h\right)-I_0\left(d^{\zeta c}r\right)K_0\left(d^{\zeta c}h\right)\right] \quad (65)$$

$$\tau_c\left(r,z\right)=-d^{\zeta c}G_c\left[C_4\sin\left(\zeta z\right)+D_4\cos\left(\zeta z\right)\right]\left[K_1\left(d^{\zeta c}b\right)I_0\left(d^{\zeta c}h\right)+I_1\left(d^{\zeta c}b\right)K_0\left(d^{\zeta c}h\right)\right] \quad (66)$$

where A_4, B_4, C_4, D_4, ζ, $d^{\zeta s}$, and $d^{\zeta c}$ are unknown coefficients and

$$d^{\zeta i}=\sqrt{\frac{2\left(1-\mu_i\right)}{1-2\mu_i}}\zeta \quad (67)$$

The boundary and continuous conditions in the frictional zone $[0, L_f]$ are as follows

$$\sigma_s\left(z=0\right) \text{ and } w_s\left(z=0\right) \text{ are continuous; } -\tau_s\left(r=a,z=0\right)=\tau_r \quad (68)$$

$$\int_0^a 2\pi r\cdot\sigma_s\left(z=L_f,r\right)\mathrm{d}r=P \quad (69)$$

$$\frac{b}{a}\tau_c\left(r=b,z\right)=\tau_s\left(r=a,z\right)=-\tau\left(z\right)=K_3\left[w_s\left(r=a,z\right)-w_c\left(r=b,z\right)-\delta_3\right] \quad (70)$$

With the conditions (68) to (70), the coefficients A_4, B_4, C_4, and D_4 are obtained as

$$A_4=\frac{\zeta d^s I_1\left(d^s a\right)}{\beta d^{\zeta s}I_1\left(d^{\zeta s}a\right)}\left[A_3\cos\left(\beta L_s\right)-B_3\sin\left(\beta L_s\right)\right];\ \ C_4=N_6A_4 \quad (71)$$

$$B_4=A_3\sin\left(\beta L_s\right)+B_3\cos\left(\beta L_s\right)+K_2-\delta_3;\ \ D_4=N_6B_4;\text{ and} \quad (72)$$

$$N_6=-\frac{ad^{\zeta s}G_sI_1\left(d^{\zeta s}a\right)}{bd^{\zeta c}G_c\left[K_1\left(d^{\zeta c}b\right)I_0\left(d^{\zeta c}h\right)+I_1\left(d^{\zeta c}b\right)K_0\left(d^{\zeta c}h\right)\right]} \quad (73)$$

Based on the condition (70), ζ can be obtained by solving the following equation

$$d^{\zeta s}G_sI_1\left(d^{\zeta s}a\right)-K_3\left\{I_0\left(d^{\zeta s}a\right)-N_6\left[K_0\left(d^{\zeta c}b\right)I_0\left(d^{\zeta c}h\right)-I_0\left(d^{\zeta c}b\right)K_0\left(d^{\zeta c}h\right)\right]\right\}=0 \quad (74)$$

The shear stress τ can be obtained by combining the condition (70) with Eq. (64)

$$\tau\left(z\right)=-d^{\zeta s}G_s\left[A_4\sin\left(\zeta z\right)+B_4\cos\left(\zeta z\right)\right]I_1\left(d^{\zeta s}a\right) \quad (75)$$

Substituting the condition (69) into Eq. (63), the load P can be expressed as

$$P=\frac{2\pi ad^{\zeta s}G_sI_1\left(d^{\zeta s}a\right)}{\zeta}\left[A_4\cos\left(\zeta L_f\right)-B_4\sin\left(\zeta L_f\right)\right] \quad (76)$$

The expression of Δ can be obtained from Eq. (61) with $r=0$ and $z=L_f$

$$\Delta=A_4\sin\left(\zeta L_f\right)+B_4\cos\left(\zeta L_f\right)+\delta_3 \quad (77)$$

Substituting $\tau(z=0)=\tau_r$ into Eq. (75) gives the relationship between L_f and L_s

$$-d^{\zeta s} G_s I_1\left(d^{\zeta s} a\right) B_4 = \tau_r \tag{78}$$

It can be seen that the load-displacement relationship can be obtained from Eqs. (76) to (78). If P_{max} occurs in this stage, it can be obtained with the Lagrange multiplier method. In particular, since the interfacial shear stress in the frictional zone remains constant, the pull-out load P can also be expressed in a simple manner from Eq. (57)

$$P = 2\pi a \tau_r L_f + \frac{2\pi a d^s G_s I_1\left(d^s a\right)}{\beta}\left[A_3 \cos\left(\beta L_s\right) - B_3 \sin\left(\beta L_s\right)\right] \tag{79}$$

where A_3 and B_3 are shown in Eqs. (49) and (50). The pull-out load P reaches the ultimate load P_{max} when the derivative of Eq. (79) is zero with respect to L_f, i.e.,

$$N_2 d_s J_1\left(d_s a\right)\left[1-\tanh^2\left(\lambda L_e\right)\right] + N_3 d_{\varphi s} J_1\left(d_{\varphi s} a\right)\left[1-\tanh^2\left(\varphi L_e\right)\right] = \frac{\tau_r}{G_s \cos\left(\beta L_s\right)} \tag{80}$$

The relationship between L_e and L_s is shown in Eq. (59), which can be further simplified as

$$\frac{N_2 d_s J_1\left(d_s a\right)\tanh\left(\lambda L_e\right)}{\lambda} + \frac{N_3 d_{\varphi s} J_1\left(d_{\varphi s} a\right)\tanh\left(\varphi L_e\right)}{\varphi} = \frac{\tau_u \cos\left(\beta L_s\right) - \tau_r}{\beta G_s \sin\left(\beta L_s\right)} \tag{81}$$

It is noted that, when the ultimate load occurs in the elastic-softening-frictional stage, the value of 'φL_e' is usually greater than 2. The reason for this is that φ is the second root of the oscillation equation (24). Thus, substituting $\tanh\left(\varphi L_e\right)=1$ into Eqs. (80) and (81) gives

$$\tanh^2\left(\lambda L_e\right) = 1 - \frac{\tau_r}{N_2 d_s G_s J_1\left(d_s a\right)\cos\left(\beta L_s\right)} \tag{82}$$

$$\tanh\left(\lambda L_e\right) = \lambda\left[\frac{\tau_u \cos\left(\beta L_s\right) - \tau_r}{N_2 \beta d_s G_s J_1\left(d_s a\right)\sin\left(\beta L_s\right)} - \frac{N_3 d_{\varphi s} J_1\left(d_{\varphi s} a\right)}{\varphi N_2 d_s J_1\left(d_s a\right)}\right] \tag{83}$$

Combination of Eq. (82) with Eq. (83) yields

$$\lambda^2\left[\frac{\tau_u \cos\left(\beta L_s\right) - \tau_r}{N_2 \beta d_s G_s J_1\left(d_s a\right)\sin\left(\beta L_s\right)} - \frac{N_3 d_{\varphi s} J_1\left(d_{\varphi s} a\right)}{\varphi N_2 d_s J_1\left(d_s a\right)}\right]^2 = 1 - \frac{\tau_r}{N_2 d_s G_s J_1\left(d_s a\right)\cos\left(\beta L_s\right)} \tag{84}$$

Thus, when the ultimate load occurs in the elastic-softening-frictional stage, the softening length L_s can be calculated from Eq. (84) with a numerical solver and the corresponding elastic length L_e can be obtained from Eq. (82) or (83). It is interesting to note that both the elastic length and the softening length are constant, independent of the bond length. In other words, if an anchorage reaches its ultimate load in the elastic-softening-frictional stage, only the frictional length L_f increases with the increase of bond length. This indicates that there exists a critical bond length, i.e., once the critical bond length is reached, the increased bond length only affects the frictional length. The effect of bond length on the ultimate load is detailed in section 6.

When the slip at the free end continues to increase, the interfacial shear stress at the free end reaches the shear strength. In this case, the elastic zone vanishes, the whole bond length is composed of the softening and frictional zones, and the interface enters the softening-frictional stage.

3.4. Softening stage

Based on the above discussions, the softening stage occurs after the elastic-softening stage when $L < L_u$. In this stage, the whole interface behaves softening. Therefore, the solutions for the softening zone Eqs. (37) to (43) are still valid by replacing A_3, B_3, C_3, and D_3 with the unknown coefficients A_5, B_5, C_5, and D_5, respectively. The boundary conditions in this stage are as follows

$$\sigma_s\left(z=0,r\right)=0\,;\quad \sigma_c\left(z=0,r\right)=0\,;\quad \int_0^a 2\pi r\cdot\sigma_s\left(z=L,r\right)\mathrm{d}r=P \tag{85}$$

$$\frac{b}{a}\tau_c\left(r=b,z\right)=\tau_s\left(r=a,z\right)=-\tau\left(z\right)=K_1\left[w_s\left(r=a,z\right)-w_c\left(r=b,z\right)-K_2\right] \tag{86}$$

With the conditions (85) and (86), the coefficients A_5, B_5, C_5, and D_5 are given by

$$A_5 = C_5 = 0\,;\;\; B_5 = -\frac{P\beta}{2\pi a d^s G_s \sin\left(\beta L\right) I_1\left(d^s a\right)};\;\; D_5 = N_5 B_5 \tag{87}$$

The shear stress τ can be obtained by substituting the condition (86) into Eq. (40)

$$\tau\left(z\right) = -d^s G_s B_5 \cos\left(\beta z\right) I_1\left(d^s a\right) \tag{88}$$

Substituting $r=0$ and $z=L$ into Eq. (37), the load-displacement relationship can be obtained as

$$\Delta = K_2 - \frac{P\beta}{2\pi a \tan\left(\beta L\right) d^s G_s I_1\left(d^s a\right)} \tag{89}$$

3.5. Softening-frictional stage

As the debonding process propagates, the softening-frictional stage occurs at the end of the elastic-softening-frictional or softening stage. In a similar manner, the solutions for the softening and frictional zones, i.e., Eqs. (37) to (43) and (61) to (67) are still valid if A_3, B_3, C_3, D_3, A_4, B_4, C_4, and D_4 are replaced with the unknown coefficients A_6, B_6, C_6, D_6, A_7, B_7, C_7, and D_7, respectively. The boundary conditions in the softening zone $[0, L_s]$ are as follows

$$\sigma_s\left(z=0\right) = 0\,;\;\; \sigma_c\left(z=0, r\right) = 0\,;\;\; -\tau_s\left(r=a, z=L_s\right) = \tau_r \tag{90}$$

$$\frac{b}{a}\tau_c\left(r=b, z\right) = \tau_s\left(r=a, z\right) = -\tau\left(z\right) = K_1\left[w_s\left(r=a, z\right) - w_c\left(r=b, z\right) - K_2\right] \tag{91}$$

Based on the above conditions, the coefficients A_6, B_6, C_6, and D_6 can be obtained as

$$A_6 = C_6 = 0\,;\;\; B_6 = -\frac{\tau_r}{d^s G_s \cos\left(\beta L_s\right) I_1\left(d^s a\right)};\;\; D_6 = N_5 B_6 \tag{92}$$

The boundary and continuous conditions in the frictional zone $[0, L_f]$ are as follows

$$\sigma_s(z=0) \text{ and } w_s(z=0) \text{ are continuous; } \int_0^a 2\pi r \cdot \sigma_s\left(z=L_f, r\right)\mathrm{dr} = P \tag{93}$$

$$\frac{b}{a}\tau_c(r=b,z) = \tau_s(r=a,z) = -\tau(z) = K_3\left[w_s(r=a,z) - w_c(r=b,z) - \delta_3\right] \tag{94}$$

The remaining unknown coefficients can be obtained from the conditions (93) and (94) as

$$A_7 = -\frac{\beta d^{\zeta s}\sin(\beta L_s) I_1\left(d^s a\right)}{\zeta d^s I_1\left(d^{\zeta s} a\right)} B_6; \quad B_7 = K_2 - \delta_3 - \frac{\tau_r}{d^s G_s I_1\left(d^s a\right)} \tag{95}$$

$$C_7 = N_6 A_7; \quad D_7 = N_6 B_7 \tag{96}$$

The shear stress τ can be formulated from the boundary conditions (91) and (94) as

$$\tau(z) = -B_6 d^s G_s \cos(\beta z) I_1\left(d^s a\right) \text{ in the softening zone } [0, L_s] \tag{97}$$

$$\tau(z) = -d^{\zeta s} G_s\left[A_7 \sin(\zeta z) + B_7 \cos(\zeta z)\right] I_1\left(d^{\zeta s} a\right) \text{ in the frictional zone } [0, L_f] \tag{98}$$

Substituting the condition (93) into Eq. (63) gives the pull-out load P

$$P = \frac{2\pi a d^{\zeta s} G_s I_1\left(d^{\zeta s} a\right)}{\zeta}\left[A_7 \cos\left(\zeta L_f\right) - B_7 \sin\left(\zeta L_f\right)\right] \tag{99}$$

The displacement at the loading point Δ is obtained from Eq. (61) as

$$\Delta = A_7 \sin\left(\zeta L_f\right) + B_7 \cos\left(\zeta L_f\right) + \delta_3 \tag{100}$$

It should be noted that in this stage, L_f is variable but can be determined within a certain range. Herein, two cases are considered. In case I, the softening-frictional stage occurs after the elastic-softening-frictional stage, while in case II the softening-frictional stage occurs after the softening stage. In case I, the elastic-softening-frictional stage ends when the length of the elastic zone reduces to zero. Substituting $z=0$ and $\tau = \tau_u$ into Eq. (97) gives

$$L_s = L_u = \frac{1}{\beta}\arccos\left(\frac{\tau_r}{\tau_u}\right); \quad L_f = L - L_u \tag{101}$$

Therefore, L_f is between $L - L_u$ and L. In case II, L_f is between 0 and L. It is worth noting that the snapback phenomenon may occur in this stage for an anchorage with a longer bond length. Snapback is caused by the sudden release of the stored strain energy in the frictional zone due to the reduced load capacity [44]. Previous studies have shown that the occurrence of snapback in the load-displacement response depends on the bond length [37, 40, 44, 45]. However, very little attention has been paid to develop theoretical formulas to evaluate the minimum bond length that exhibits snapback. In this regards, the present study details the derivation of the minimum bond length as follows.

As previously mentioned, the softening-frictional stage occurs after the elastic-softening-frictional stage once the elastic zone vanishes. It follows from Eq. (101) that $L_s = L_u$ and $L_f = L - L_u$. In this case, the displacement at the loading point Δ_1 can be obtained by substituting $L_s = L_u$ and $L_f = L - L_u$ into Eq. (100) as

$$\Delta_1 = A_8 \sin\left[\zeta\left(L - L_u\right)\right] + B_8 \cos\left[\zeta\left(L - L_u\right)\right] + \delta_3 \tag{102}$$

where

$$A_8 = -\frac{\tau_u \zeta \sin\left(\beta L_u\right)}{\beta d^{\zeta s} G_s I_1\left(d^{\zeta s} a\right)}; \quad B_8 = B_7 = K_2 - \delta_3 - \frac{\tau_r}{d^s G_s I_1\left(d^s a\right)} \tag{103}$$

On the other hand, the softening-frictional stage ends when the softening length vanishes, i.e., $L_s = 0$ and $L_f = L$. In this case, the displacement at the loading point Δ_2 can be obtained by substituting $L_s = 0$ and $L_f = L$ into Eq. (100) as

$$\Delta_2 = B_7 \cos\left(\zeta L\right) + \delta_3 \tag{104}$$

It follows from $\Delta_1 = \Delta_2$ that

$$A_8 \sin\left[\zeta\left(L - L_u\right)\right] + B_8 \left\{\cos\left[\zeta\left(L - L_u\right)\right] - \cos\left(\zeta L\right)\right\} = 0 \tag{105}$$

It can be seen from Eq. (105) that the minimum bond length L_{sn} that exhibits snapback can be determined from Eq. (105) using a mathematical solver. The significance of L_{sn} is that it is the shortest bond length that exhibits snapback phenomenon, which may lead to a catastrophic bond failure and become more dangerous as the bond length increases [45].

Afterwards, the whole interface enters the frictional stage when the softening zone vanishes. In this case, the interfacial shear stress remains constant and the pull-out load P is independent of the slip. For convenience, the solutions in the frictional stage are given in the Appendix.

4. Anchor pull-out response and interfacial bond behavior

Consider a typical anchor system, in which a steel thread bar is embedded in concrete with cement grout [9]. The material properties and geometric and interfacial parameters are taken from the pull-out test of Benmokrane et al. [9] as follows: $E_s = 205\,\text{GPa}$, $E_c = 30\,\text{GPa}$, $G = 7.7826\,\text{GPa}$, $\mu_s = 0.3$, $\mu_c = 0.2$, $a = 7.9$ mm, $b = 19$ mm, $h = 100$ mm, $\tau_u = 14.5$ MPa, $\delta_1 = 2.9$ mm, $\tau_r = 3.7$ MPa, $\delta_2 = 10.6$ mm, and $\delta_3 = 100\delta_2 = 1060$ mm. With these parameters, the value of L_u can be obtained from Eq. (60) as 1156 mm. To study the pull-out response of the anchor and the interfacial bond behavior during the whole pull-out process for different bond lengths, the load-displacement curves and the interfacial shear stress distributions for L smaller, equal to, or larger than L_u are considered.

4.1. Load-displacement curves

When the bond length is smaller than L_u, two bond lengths of 100 and 800 mm are considered. The load-displacement curve for $L = 100$ mm is shown in Fig. 5(a). It can be seen from Fig. 5(a) that the branch O-A obtained from Eq. (26) is linear elastic and terminates when P reaches the elastic ultimate load P_e. Subsequently, the elastic-softening stage, i.e., the branch A-B obtained by Eqs. (57) and (58), is non-linear. This cannot be clearly observed in

Fig. 5(a) since the interfacial shear stress distributes uniformly along the bond length. Afterwards, the response in the softening stage, i.e., branch B-C obtained from Eq. (89), is linear. It is noted that the softening-frictional stage may not happen due to the uniform shear stress distribution, as shown in Fig. 5(a). The load-displacement curve in the frictional stage is represented by the horizontal line C-D obtained from Eq. (A.5).

The load-displacement curve for $L = 800$ mm is illustrated in Fig. 5(b). Beyond P_e (point A), the load increases with the extension of softening zone. Afterwards the ultimate load P_{max} (point B) is reached and the curve exhibits a nonlinearly decreasing trend (branch B-C). The branch C-D represents the softening stage and terminates when the frictional zone starts to develop from the loaded end. The branch D-E, corresponding to the softening-frictional stage, can be obtained from Eqs. (99) and (100).

Fig. 5(c) shows the load-displacement curve for $L = L_u$. As in the last case, the interface behaves elastically until P_e is reached. With the propagation of softening zone, the load increases nonlinearly until the ultimate load P_{max} is reached. Afterwards, the non-linear softening response occurs and terminates at the point C, where the softening length is equal to the bond length, i.e., $L_s = L_u = L$ and τ at the loaded end is equal to τ_r. Subsequently, the softening-frictional stage occurs after the elastic-softening stage, corresponding to the non-linear branch C-D.

The load-displacement curve for $L = 2000$ mm is shown in Fig. 5(d). The branches O-A and A-B represent the elastic and elastic-softening stages, respectively. The branch B-C-D corresponds to the elastic-softening-frictional stage and can be obtained from Eqs. (76) to (78). It is noted that, in this stage, the load P first reaches the ultimate load P_{max} (point C) and thereafter decreases gradually until the elastic zone vanishes. The reason for this is that, when the frictional zone extends to a certain extent, the loss of pull-out capacity in the elastic zone may be larger than the resistance force provided by the frictional zone. Afterwards, the softening-frictional stage occurs, which corresponds to the snapback branch D-E and is very challenging to be captured in any displacement controlled or load controlled pull-out test [44, 45].

4.2. Interfacial shear stress distribution

The interfacial shear stress distribution for $L = 100$ mm is illustrated in Fig. 6(a). It can be clearly seen from Fig. 6(a) that the shear stress successively appears at four different stages, i.e., elastic, elastic-softening, softening, and frictional stages, which can be obtained from Eqs. (25), (55) and (56), (88), and (A.4), respectively. A uniform distribution throughout the pull-out process is observed, indicating that pull-out tests with short bond lengths can be used to derive the bond-slip model.

As for $L = 800$ mm shown in Fig. 6(b), five pull-out stages can be found. In the elastic stage, τ increases non-linearly along the bond length. In the elastic-softening stage, however, τ increases with increasing z in the elastic zone but decreases with decreasing z in the softening zone. Afterwards, the softening stage occurs and τ gradually decreases until it reduces to τ_r at the loaded end. In the softening-frictional stage, Eqs. (97) and (98) are adopted to obtain the interfacial shear stress distribution.

The interfacial shear stress distribution for $L = L_u$ is depicted in Fig. 6(c). At the end of the elastic-softening stage, τ at the free end increases to τ_u while τ at the loaded end reduces to τ_r. The softening-frictional stage occurs after the elastic-softening stage. Fig. 6(d) represents the interfacial shear stress distribution for $L = 2000\ \text{mm}$. Compared with the case for $L = 800\ \text{mm}$, the failure process experiences an elastic-softening-frictional stage, in which the shear stress distribution can be obtained from Eqs. (55), (56), and (75).

From the above discussions, it is seen that the bond length L determines the possible stages that occur during the pull-out process. For short bond lengths such as $L = 100\ \text{mm}$, the interfacial shear stress distribution is uniform along the bond length and therefore the shape of the load-displacement curve depicted in Fig. 5(a) is analogous to that of the bond-slip model. However, the non-uniform shear stress distribution becomes more pronounced as the bond length increases, which can be clearly observed from Fig. 6.

5. Experimental verifications

The experiments herein presented refer to laboratory pull-out tests, whose numerous results have been reported in the literature. To verify the efficiency of the proposed analytical model, four series of laboratory pull-out tests are collected for comparison. It is noted that, although the outer boundaries in these pull-out tests are unconstrained, the axial stiffnesses of the test samples are large enough so that the deformations at the outer boundaries can be assumed to be zero. Thus, the test results can be used for comparison with the analytical model.

The first pull-out test, regarding cable bolts embedded in concrete cylinders with plain cement grouts, was reported by Rajaie [46]. The parameters were as follows: $a = 7.6\ \text{mm}$, $b = 25.5\ \text{mm}$, $h = 125\ \text{mm}$, $G = 8.9076\ \text{GPa}$, $E_s = 194\ \text{GPa}$, $\mu_s = 0.3$, $E_c = 19\ \text{GPa}$, and

$\mu_c = 0.2$. The interfacial parameters were determined by pull-out tests for $L = 200$ mm as: $\tau_u = 5.84$ MPa, $\tau_r = 2.81$ MPa, $\delta_1 = 9.9$ mm, and $\delta_2 = 19.9$ mm. The bond length varied from 150 to 700 mm. With these parameters known, the ultimate load P_{max} with different bond lengths can be obtained, as listed in Table 1, together with the measured P_{emax}. From Table 1, it can be seen that the analytical solution agrees well with the test results, indicating that the analytical solution is able to predict the ultimate load of grouted anchors.

The second pull-out test was conducted by Chen et al. [47]. The anchor was a modified cable bolt and embedded in a commercial cement grout with strata binder grout. The parameters were as follows: $a = 14.25$ mm, $b = 21$ mm, $h = 175$ mm, $G = 4.1074$ GPa, $E_s = 201$ GPa, $\mu_s = 0.3$, $E_c = 11.82$ GPa, and $\mu_c = 0.2$. The pull-out test for $L = 320$ mm was used to calibrate the interfacial parameters: $\tau_u = 13.50$ MPa, $\tau_r = 11.00$ MPa, $\delta_1 = 5.0$ mm, and $\delta_2 = 12.0$ mm. With these parameters, the ultimate loads with bond lengths of 320 to 380 mm can be obtained as shown in Table 2, together with the test results of Chen et al. [47]. It is seen from Table 2 that the proposed analytical solution is in good agreement on the test results, which further validates the accuracy of the analytical model.

Zhang et al. [19] performed a series of pull-out tests on FRP rods embedded in steel tubes with cement grout. Three types of FRP rods, round sanded (FR1), spiral wound (FR2), and indented (FR3), and four types of cement grouts, CG1, CG2, CG3, and CG4, were adopted. The radii and Poisson's ratios of FRP rods and the shear moduli of cement grouts were as follows: $a = 3.75$ mm, $\mu_s = 0.38$ for FR1; $a = 4.00$ mm, $\mu_s = 0.35$ for FR2; and $a = 3.95$ mm, $\mu_s = 0.38$ for FR3 and $G = 7.8378$, 8.3784, 10.4091 and 7.4554 GPa for CG1, CG2, CG3, and CG4, respectively. For each specimen, the parameters were as follows:

$b = 25.5\ \mathrm{mm}$, $h = 28.5\ \mathrm{mm}$, $E_c = 195\ \mathrm{GPa}$, and $\mu_c = 0.3$. Detailed information regarding the other parameters is shown in Table 3. Based on the analytical model, the ultimate load for each specimen can be obtained as listed in Table 3, together with the experiment results. It can be seen from Table 3 that, the proposed analytical model agrees well with the experimental results except for specimens 5, 6, and 12. The reason for this is that the three types of FRP rods have lower Young's moduli and longer bond lengths, resulting in a significant radial deformation in the FRP rods under a larger pull-out load, which is not considered in the proposed analytical model.

The pull-out test on FRP tendons embedded in cement mortar filled steel tubes conducted by Zhang and Benmokrane [20] is used to further verify the proposed analytical model. In their test, two types of FRP tendons, round sanded (AR) and Leadline ribbed (LE), and two types of cement grouts, CM and EM, were used. The radii and Young's moduli of FRP tendons were 3.75 mm and 60.8 GPa for AR and 3.95 mm and 163.3 GPa for LE. The shear moduli of cement grouts were 9.1129 and 10.9016 GPa for EM and CM, respectively. For each specimen, the parameters were as follows: $b = 25.5\ \mathrm{mm}$, $h = 28.5\ \mathrm{mm}$, $\mu_s = 0.38$, $E_c = 195\ \mathrm{GPa}$, and $\mu_c = 0.3$. The other parameters are listed in Table 4. Thus, the ultimate load can be predicted as shown in Table 4, together with the experimental results. It can be seen from Table 4 that the analytical solution is in good agreement with the experimental results. The interfacial shear stress distribution along the bond length at the ultimate state is shown in Fig. 7. It is seen from Fig. 7 that the shear stress is uniform along the bond length since the bond length of each specimen is relatively short. Thus, the interfacial parameters measured by experiments are reliable.

In order to further validate the proposed analytical model, the load-displacement responses of different specimens are calculated and compared with the experimental results of Zhang and Benmokrane [20], as shown in Fig. 8. It can be seen from the experimental curves shown in Fig. 8 that, after the ultimate load is reached, the response exhibits a sharp decrease in pull-out load with an increase in slip, indicating that the bond property of the anchorage may degrade due to the propagation of interfacial cracking. It is noted that from this point onwards, the experimental response exhibits an oscillating residual pull-out capacity due to the mechanical interlocking between Leadline ribbed tendons and grout [20].

The predicted load-displacement curves are also shown in Fig. 8 for different consecutive debonding stages, where A, B, C, and D represent the ends of the elastic, elastic-softening, softening, and softening-frictional stages, respectively. It can be seen from the analytical curves shown in Fig. 8 that, after the peak load, the interface starts to transfer from the elastic-softening stage (branch A-B) to the softening stage (branch B-C) since the bond lengths of the three specimens are much smaller than L_u. As debonding propagates, the interface enters the softening-frictional stage (branch C-D), in which debonding initiates at the loaded end and propagates rapidly towards the free end. Finally, the interface enters the complete frictional stage, which is followed by the gradual pull-out of grouted tendons. It should be noted that from the point D onwards, the predicted pull-out load remains constant and therefore is not in good agreement with the experimental results. This inconsistency could be explained as follows. Since the three FRP tendons are Leadline ribbed, the grout flutes are crushed, and the tendon ribs are partially sheared off during the pull-out process [20]. As a result, the experimental response exhibits an oscillation in the residual load due to the mechanical interlocking between the tendon ribs and grout. However, the effect of anchor profile configuration on the interfacial bond failure is not taken into account in the present model and the tri-linear bond-slip model with constant frictional stress is used to describe the interaction between the anchor and grout.

Besides, it is interesting to note that the predicted load-displacement response approaches to that of the local bond-slip model shown in Fig. 2. The reason for this is that the interfacial shear stress distribution is almost uniform for anchorages with short bond lengths, as shown in Fig. 7. From the above discussions, it is seen that the present analytical model is capable of predicting the ultimate load capacity and the load-displacement response of grouted anchors.

6. Effect of bond length

It can be seen from the proposed analytical solution that the bond length exhibits an important effect on the pull-out behavior of grouted anchors. Therefore, it is of practical significance to investigate its effect on the ultimate load and the load-displacement response. The parameters of the test of Benmokrane et al. [9] as given in section 4 are used as the reference values.

The effect of bond length L on the ultimate load P_{max} is shown in Fig. 9(a), which shows that, as the bond length increases, P_{max} increases rapidly. However, when the bond length exceeds around 1300 mm, P_{max} increases at a much lower but steady rate. This confirms the presence of a critical bond length L_{cri}, as marked by the black dot in Fig. 9(a). The reason for this is that, the ultimate load P_{max} appears in the elastic-softening stage when L is smaller than

L_{cri}. Otherwise, P_{max} occurs in the elastic-softening-frictional stage. As discussed in section 3.3 as seen from Eqs. (79) to (84), if P_{max} appears in the elastic-softening-frictional stage, the elastic and softening lengths are constant and only the frictional length increases with the increase of bond length. Since the interfacial shear stress in the frictional zone keeps a constant value τ_r smaller than that in any other part of the anchorage, the increase of bond length has a smaller but steady influence on P_{max} once it is larger than L_{cri}. The method for determining the value of L_{cri} is described as follows. When P_{max} occurs in the elastic-softening-frictional stage, the elastic length L_e and softening length L_s can be obtained from Eqs. (83) and (84) without knowing the bond length in advance. Thus, L_{cri} is equal to the sum of L_e and L_s. For example, with the parameters taken in this section, L_e, L_s, and L_{cri} are calculated as 445, 838, and 1293 mm, respectively, which is consistent with the observation shown in Fig. 9(a).

The effect of bond length on the load-displacement curve is shown in Fig. 9(b). It can be seen from Fig. 9(b) that the bond length has a significant influence on the load-displacement response of anchorages. With the parameters taken in this section, the minimum bond length that exhibits snapback can be obtained from Eq. (105) as $L_{sn} = 1462\ \mathrm{mm}$. As expected, when L is less than L_{sn}, no snapback occurs and the load-displacement curves show a postpeak softening response. Moreover, Fig. 9(b) shows that an increase in bond length beyond L_{sn} leads to an increase in the intensity of snapback. In other words, the snapback response becomes more pronounced as the bond length increases. This can be explained as follows. Fig. 9(a) shows that, for a bond length greater than L_{sn} ($> L_{cri}$), the frictional length increases with the increase of bond length. As a result, the longer the bond length is, the larger the amount of strain energy in the frictional zone is stored. Thus, as the bond length increases, the frictional zone releases more stored strain energy, which results in an increase in the intensity of snapback and the ductility of the failure process.

7. Conclusions

This paper has presented a three-dimensional analytical model for the nonlinear pull-out response of anchorage systems based on a tri-linear interfacial bond-slip relationship. Due to the axisymmetric nature of anchorages, the proposed analytical model is able to provide a rigorous and complete theoretical basis for understanding the debonding mechanism and for predicting the full-range pull-out behavior of anchorages. Based on this study, the following conclusions can be made as follows:

(1) Three-dimensional analytical solutions have been derived for the stress field, displacement field, and load-displacement response of anchorage systems during the whole complete pull-out process.

(2) By comparing with experimental data, it has been validated that the proposed analytical model is capable of predicting the ultimate pull-out load and load-displacement response of grouted anchors.

(3) It has been found that there exists a minimum bond length L_u which is responsible for all possible pull-out stages during the process of debonding.

(4) The ultimate load P_{max} increases rapidly with the increase of bond length before the critical bond length L_{cri} is reached but thereafter at a small but steady rate.

(5) The observed snapback in the load-displacement response is dependent on the bond

length. Anchorage systems with bond lengths shorter than L_{sn} do not exhibit snapback. Otherwise, snapback becomes more pronounced with an increase in bond length.

Acknowledgements

The financial support from the National Natural Science Foundation of China with grant No. 51421064 and the partial financial support from the United Kingdom Royal Academy of Engineering through the Distinguished Visiting Fellow scheme with grant No. DVF1617_5_21 are gratefully acknowledged.

References

[1] Cai Y, Esaki T, Jiang YJ. An analytical model to predict axial load in grouted rock bolt for soft rock tunnelling. Tunn Undergr Space Technol 2004; 19(6): 607-18.

[2] Wang DP, Wu DS, He SM, Zhou J, Ouyang CJ. Behavior of post-installed large-diameter anchors in concrete foundations. Constr Build Mater 2015; 95: 124-32.

[3] Zhang MY, Zhang J, Liu JW, Zhao HF. Experimental investigation on anti-floating anchor in moderately weathered granite. Chi J Rock Mech Eng 2008; 27: 2741-6.

[4] Zhao YM, Yang MJ. Pull-out behavior of an imperfectly bonded anchor system. Int J Rock Mech Min Sci 2011; 48(3): 469-75.

[5] Cook RA. Behavior of chemically bonded anchors. J Struct Eng ASCE 1993; 119(9): 2744-62.

[6] Cook RA, Kunz J, Fuchs W, Konz RC. Behavior and design of single adhesive anchors under tensile load in uncracked concrete. ACI Struct J 1998; 95(1): 9-26.

[7] James RW, Guardia CD, McGreary Jr CR. Strength of epoxy-grouted anchor bolts in concrete. J Struct Eng ASCE 1987; 113(12): 2365-81.

[8] Zamora NA, Cook RA, Konz RC, Consolazio GR. Behavior and design of single, headed and unheaded, grouted anchors under tensile load. ACI Struct J 2003; 100(2): 222-30.

[9] Benmokrane B, Chennouf A, Mitri HS. Laboratory evaluation of cement-based grouts and grouted rock anchors. Int J Rock Mech Min Sci 1995; 32(7): 633-42.

[10] Farmer IW. Stress distribution along a resin grouted rock anchor. Int J Rock Mech Min Sci Geomech Abstr 1975; 12(11): 347-51.

[11] Hoek E, Wood DF. Rock support. Int J Rock Mech Min Sci Geomech Abstr 1989; 26: 282-7.

[12] Kaiser PK, Yazici S, Nose J. Effect of stress change on the bond strength of fully grouted cables. Int J Rock Mech Min Sci Geomech Abstr 1992; 29(3): 293-306.

[13] Benmokrane B, Xu H, Bellavance E. Bond strength of cement grouted glass fibre reinforced plastic (GFRP) anchor bolts. Int J Rock Mech Min Sci Geomech Abstr 1996; 33(5): 455-65.

[14] Cao C, Ren T, Zhang YD, Zhang L, Wang FT. Experimental investigation of the effect of grout with additive in improving ground support. Int J Rock Mech Min Sci 2016; 85: 52-9.

[15] Chen, JH, Hagan PC, Saydam S. Parametric study on the axial performance of a fully grouted cable bolt with a new pull-out test. Int J Min Sci Technol 2016; 26(1): 53-8.

[16] Chen, JH, Hagan PC, Saydam S. Sample diameter effect on bonding capacity of fully grouted cable bolts. Tunn Undergr Space Technol 2017; 68: 238-43.

[17] Colak A. Parametric study of factors affecting the pull-out strength of steel rods bonded into precast concrete panels. Int J Adhes Adhes 2001; 21(6): 487-93.

[18] Kılıc A, Yasar E, Celik AG. Effect of grout properties on the pull-out load capacity of fully grouted rock bolt. Tunn Undergr Space Technol 2002; 17(4): 355-62.

[19] Zhang BR, Benmokrane B, Chennouf A. Prediction of tensile capacity of bond anchorages for FRP tendons. J Compos Constr ASCE 2000; 4(2): 39-47.

[20] Zhang BR, Benmokrane B. Pullout bond properties of fiber-reinforced polymer tendons to grout. J Mater Civ Eng ASCE 2002; 14(5): 399-408.

[21] Ma SQ, Nemcik J, Aziz N. An analytical model of fully grouted rock bolts subjected to tensile load. Constr Build Mater 2013; 49: 519-26.

[22] Zheng JJ, Dai JG. Prediction of the nonlinear pull-out response of FRP ground anchor using an analytical transfer matrix method. Eng Struct 2014; 81: 377-85.

[23] Yang ST, Wu ZM, Hu XZ, Zheng JJ. Theoretical analysis on pullout of anchor from anchor–mortar–concrete anchorage system. Eng Fract Mech 2008; 75(5): 961-85.

[24] Wu ZM, Yang ST, Hu XZ, Zheng JJ. Analytical method for pullout of anchor from anchor–mortar–concrete anchorage system due to shear failure of mortar. J Eng Mech ASCE 2007; 133(12): 1352-69.

[25] Wu ZM, Yang ST, Wu YF, Hu XZ. Analytical method for failure of anchor-grout-concrete anchorage due to concrete cone failure and interfacial debonding. J Struct Eng ASCE 2009; 135(4): 356-65.

[26] Wu ZM, Yang ST, Zheng JJ, Hu XZ. Analytical solution for the pull-out response of FRP rods embedded in steel tubes filled with cement grout. Mater Struct 2010; 43(5): 597-609.

[27] Zheng JJ, Dai JG. Analytical solution for the full-range pull-out behavior of FRP ground anchors. Constr Build Mater 2014; 58: 129-37.

[28] Ren FF, Yang ZJ, Chen JF, Chen WW. An analytical analysis of the full-range behaviour of grouted rockbolts based on a tri-linear bond-slip model. Constr Build Mater 2010; 24(3): 361-70.

[29] Chen JH, Saydam S, Hagan PC. An analytical model of the load transfer behavior of fully grouted cable bolts. Constr Build Mater 2015; 101: 1006-15.

[30] Ma SQ, Zhao ZY, Nie W, Zhu X. An analytical model for fully grouted rockbolts with consideration of the pre-and post-yielding behavior. Rock Mech Rock Eng 2017; 50(11): 3019-28.

[31] Saleem M, Tsubaki T. Multi-layer model for pull-out behavior of post-installed anchor. In: Proceedings FRAMCOS-7, Fracture Mechanics of Concrete Structures; Aedificatio, Germany. 2010. Vol. 2, pp. 823-830.

[32] Saleem M, Tsubaki T. Two-layer model for pull-out behavior of post-installed anchor. J Jpn Soc Civ Eng, Ser E2 Mater Concr Struct 2012; 68(1): 49-62.

[33] Saleem M. Cyclic pull-out push-in shear-lag model for post-installed anchor-infill assembly. Ar J Sci Eng 2014; 39(12): 8537-8547.

[34] Saleem M, Nasir M. Bond evaluation of steel bolts for concrete subjected to impact loading. Mater Struct 2016; 49(9): 3635-3646.

[35] Saleem M. Cyclic Shear-Lag Model of Steel Bolt for Concrete Subjected to Impact Loading. J Mater Civ Eng ASCE 2018; 30(3): 04018023.

[36] Saleem M. Multiple crack extension model of steel anchor bolts subjected to impact loading. Constr Build Mater 2018; 180: 364-374.

[37] Huang P, Sun Y, Mei K, et al. A theoretical solution for the pullout properties of a single FRP rod embedded in a bond type anchorage. Mech Adv Mater Struct 2018; 1-14.

[38] Lahouar, M. A., Pinoteau, N., Caron, J. F., Foret, G., and Mege, R. A nonlinear shear-lag model applied to chemical anchors subjected to a temperature distribution. Int J Adhes Adhes 2018; 84: 438-450.

[39] Caggiano, A., Martinelli, E., and Faella, C. A fully-analytical approach for modelling the

response of FRP plates bonded to a brittle substrate. Int J Solids Struct 2012; 49(17): 2291-2300.

[40] Vaculik, J., Sturm, A. B., Visintin, P., and Griffith, M. C. Modelling FRP-to-substrate joints using the bilinear bond-slip rule with allowance for friction—Full-range analytical solutions for long and short bonded lengths. Int J Solids Struct 2018; 135: 245-260.

[41] Prieto-Muñoz PA, Yin HM, Testa RB. Mechanics of an adhesive anchor system subjected to a pullout load. I: Elastic analysis. J Struct Eng ASCE 2013; 140(2): 04013052.

[42] Prieto-Muñoz PA, Yin HM, Testa RB. Mechanics of an adhesive anchor system subjected to a pullout load. II: Viscoelastic analysis. J Struct Eng ASCE 2013; 140(2): 04013053.

[43] Upadhyaya P, Kumar S. Pull-out capacity of adhesive anchors: An analytical solution. Int J Adhes Adhes 2015; 60: 54-62.

[44] Carrara, P., Ferretti, D., Freddi, F., and Rosati, G. Shear tests of carbon fiber plates bonded to concrete with control of snap-back. Eng Fract Mech 2011; 78(15): 2663-2678.

[45] Ali-Ahmad, M. K., Subramaniam, K. V., and Ghosn, M. Analysis of scaling and instability in FRP-concrete shear debonding for beam-strengthening applications. J Eng Mech ASCE 2007; 133(1): 58-65.

[46] Rajaie H. Experimental and numerical investigations of cable bolt support systems. Ph.D. dissertation, McGill University; 1990.

[47] Chen JH, Saydam S, Hagan PC. Axial performance of a fully grouted modified cable bolt tested with a new laboratory short encapsulation pull test. In: Proceedings of the 34th International Conference on Ground Control in Mining; Morgantown, USA. 2015. pp. 1-8.

Appendix

Closed-form solutions for frictional stage

When the interfacial shear stress τ at the free end reduces to τ_r, the whole interface exhibits only friction. Thus, the solutions for the frictional zone Eqs. (61) to (67) are valid by replacing A_4, B_4, C_4, and D_4 with the unknown coefficients A_9, B_9, C_9, and D_9, respectively. The boundary conditions are as follows

$$\sigma_s\left(z=0,r\right)=0\,;\;\; \sigma_c\left(z=0,r\right)=0\,;\;\; \int_0^a 2\pi r\cdot\sigma_s\left(z=L,r\right)\mathrm{d}r=P \tag{A.1}$$

$$\frac{b}{a}\tau_c\left(r=b,z\right)=\tau_s\left(r=a,z\right)=-\tau\left(z\right)=K_3\left[w_s\left(r=a,z\right)-w_c\left(r=b,z\right)-\delta_3\right] \tag{A.2}$$

Substituting the conditions (A.1) and (A.2) into Eqs. (61) to (67), the coefficients A_9, B_9, C_9, and D_9 can be obtained as

$$A_9=C_9=0\,;\;\; B_9=-\frac{P\zeta}{2\pi a d^{\zeta s}G_s\sin\left(\zeta L\right)I_1\left(d^{\zeta s}a\right)}\,;\;\; D_9=N_6B_9 \tag{A.3}$$

The interfacial shear stress τ can be obtained from the condition (A.2) as

$$\tau\left(z\right)=\frac{P\zeta\cosh\left(\zeta z\right)}{2\pi a\sinh\left(\zeta L\right)} \tag{A.4}$$

Substituting $r=0$ and $z=L$ into Eq. (61) gives the load-displacement relationship

$$\Delta=\delta_3-\frac{P\zeta}{2\pi a\tanh\left(\zeta L\right)d^{\zeta s}G_sI_1\left(d^{\zeta s}a\right)} \tag{A.5}$$

It should be noted that the interfacial shear stress τ in the frictional stage remains a constant value τ_r along the bond length. Since the slip δ_3 is assumed to be extremely larger than δ_2 in the current study, the shear stress solved from Eq. (A.4) can be considered as constant in a smaller range.

List of figure and table captions

Fig. 1. Anchor-mortar-concrete anchorage.

Fig. 2. Bond stress-slip relationship in (a) typical tri-linear model and (b) tri-linear model used in this paper.

Fig. 3. Stress analysis of mortar cylindrical shell element.

Fig. 4. Various possible debonding cases at anchor-mortar interface.

Fig. 5. Load-displacement curves for (a) L=100 mm, (b) L=800 mm, (c) L=1156 mm, and (d) L=2000 mm.

Fig. 6. Interfacial shear stress distributions for (a) L=100 mm, (b) L=800 mm, (c) L=1156 mm, and (d) L=2000 mm.

Fig. 7. Interfacial shear stress distributions along bond length at ultimate state for (a) specimens AREM40 and AREM80, (b) specimens LECM40 and LECM80, and (c) specimens LEEM40 and LEEM80.

Fig. 8. Comparison of load-displacement curve between analytical solution and experimental results for (a) specimen LECM40, (b) specimen LECM80, and (c) specimen LEEM 80.

Fig. 9. Effect of bond length on (a) ultimate load and (b) load-displacement curve.

Table 1 Comparison of ultimate load between analytical solution and experimental results of Rajaie [46].

Table 2 Comparison of ultimate load between analytical solution and experimental results of Chen et al. [47].

Table 3 Comparison of ultimate load between analytical solution and experimental results of

Zhang et al. [19].

Table 4 Comparison of ultimate load between analytical solution and experimental results of Zhang and Benmokrane [20].

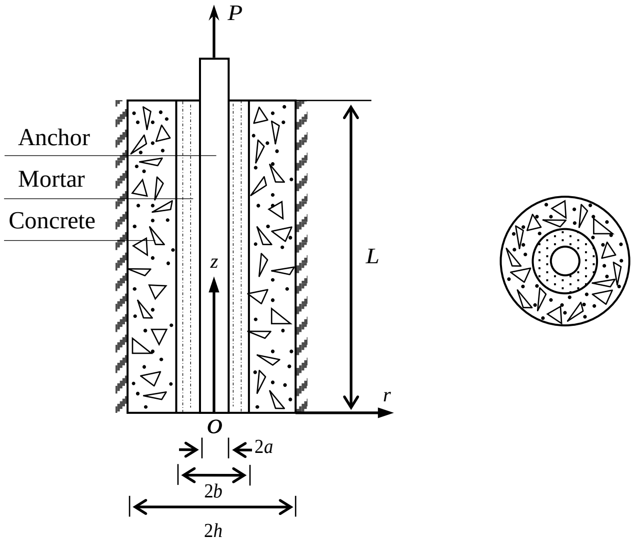

Fig. 1. Anchor-mortar-concrete anchorage.

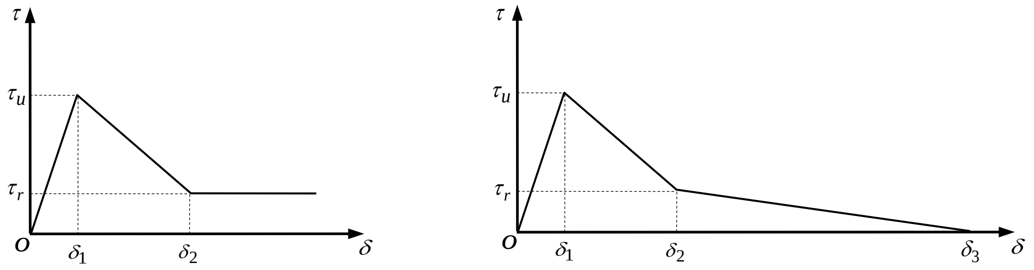

(a) (b)

Fig. 2. Bond stress-slip relationship in (a) typical tri-linear model and (b) tri-linear model used in this paper.

857 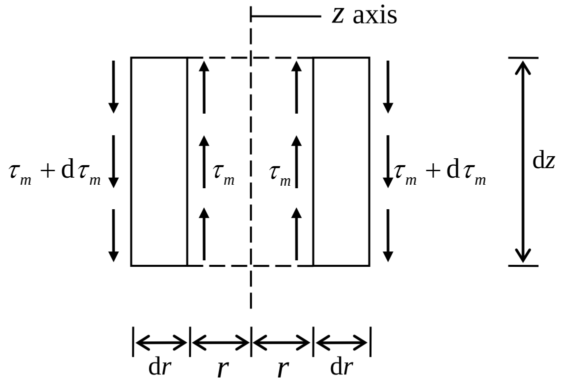

858 **Fig. 3.** Stress analysis of mortar cylindrical shell element.

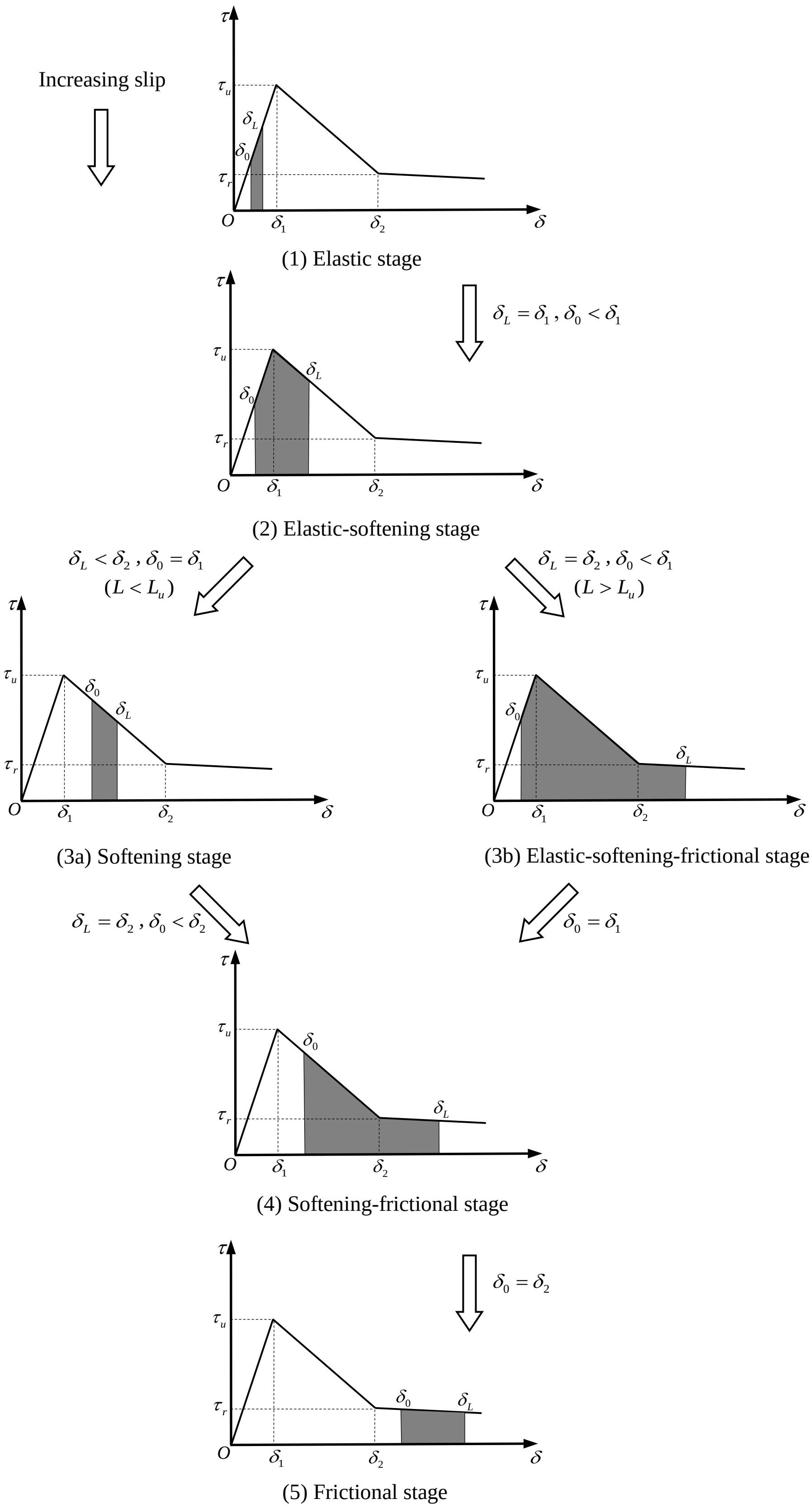

Fig. 4. Various possible debonding cases at anchor-mortar interface.

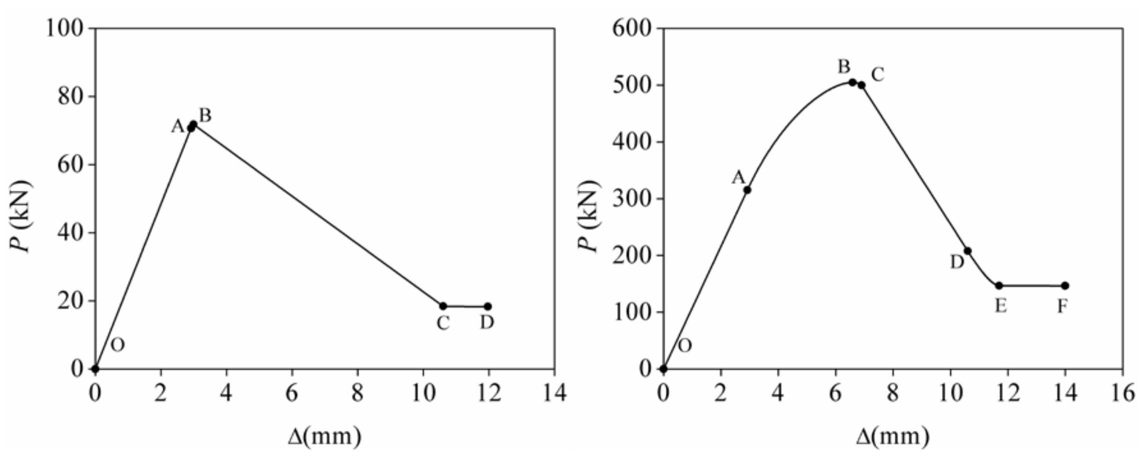

(a) (b)

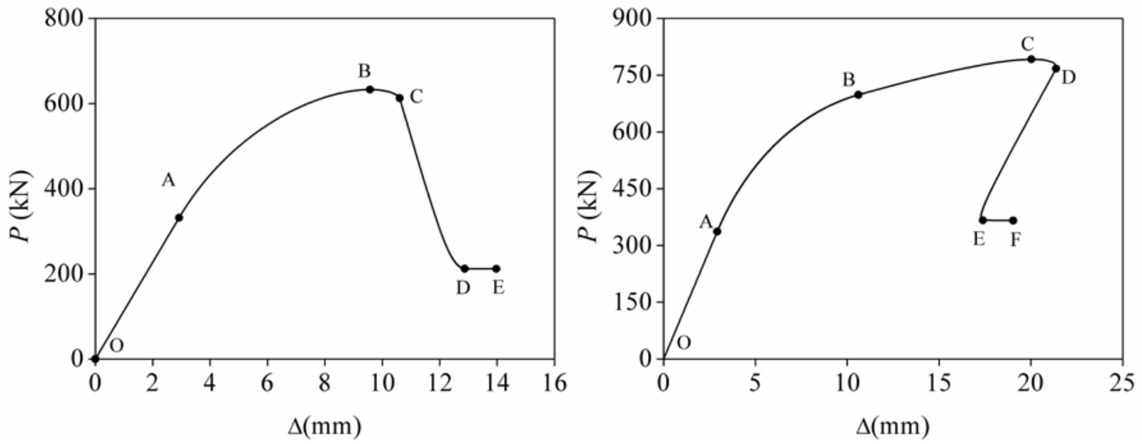

(c) (d)

Fig. 5. Load-displacement curves for (a) *L*=100 mm, (b) *L*=800 mm, (c) *L*=1156 mm, and (d) *L*=2000 mm.

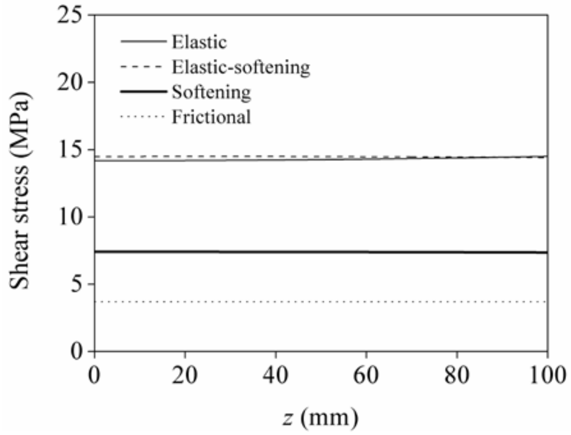

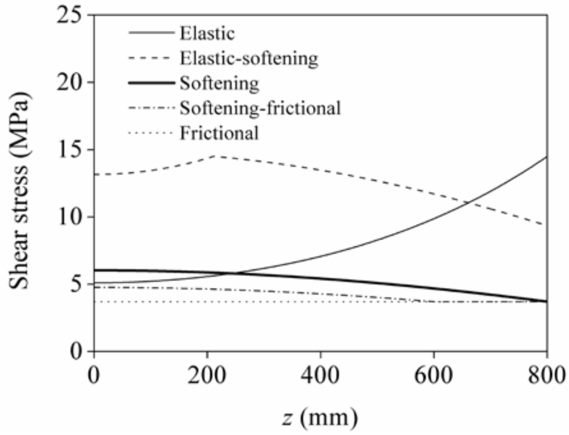

(a) (b)

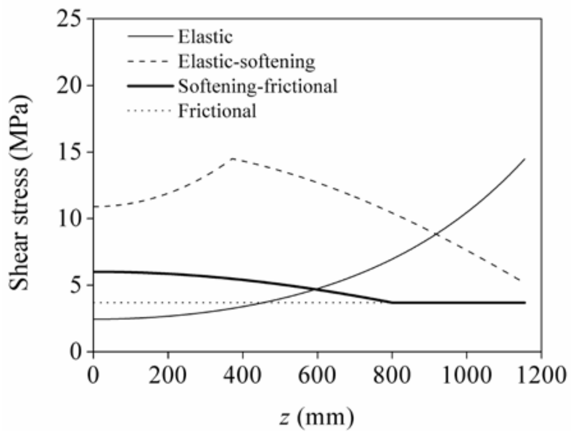

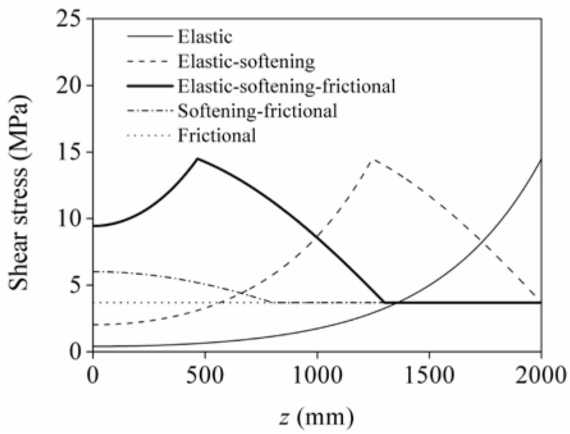

(c) (d)

Fig. 6. Interfacial shear stress distributions for (a) L=100 mm, (b) L=800 mm, (c) L=1156 mm, and (d) L=2000 mm.

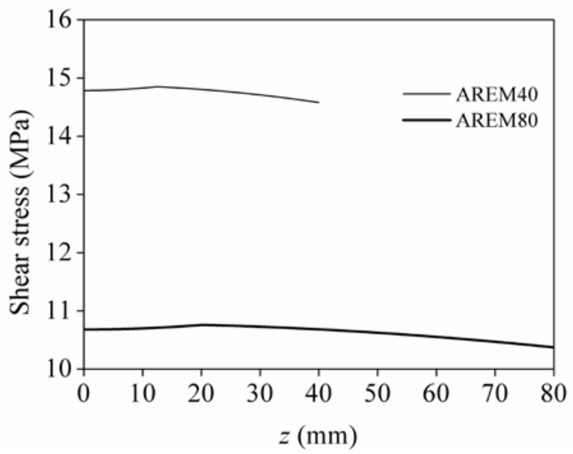

(a)

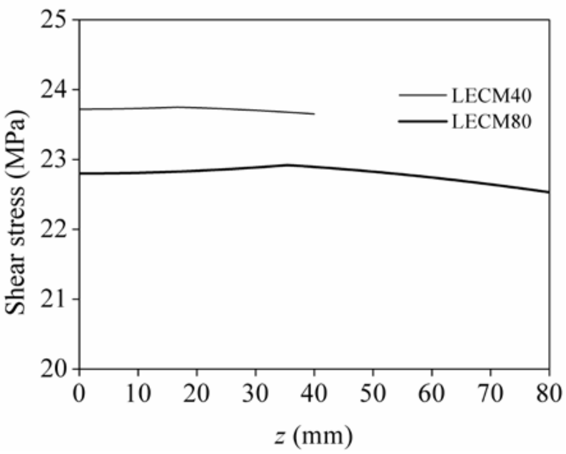

(b)

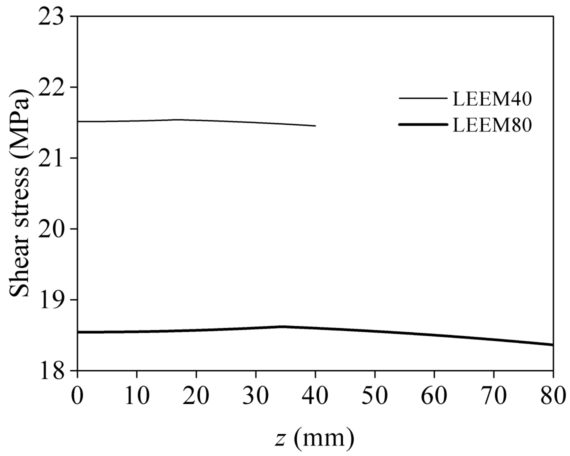

(c)

Fig. 7. Interfacial shear stress distributions along bond length at ultimate state for (a) specimens AREM40 and AREM80, (b) specimens LECM40 and LECM80, and (c) specimens LEEM40 and LEEM80.

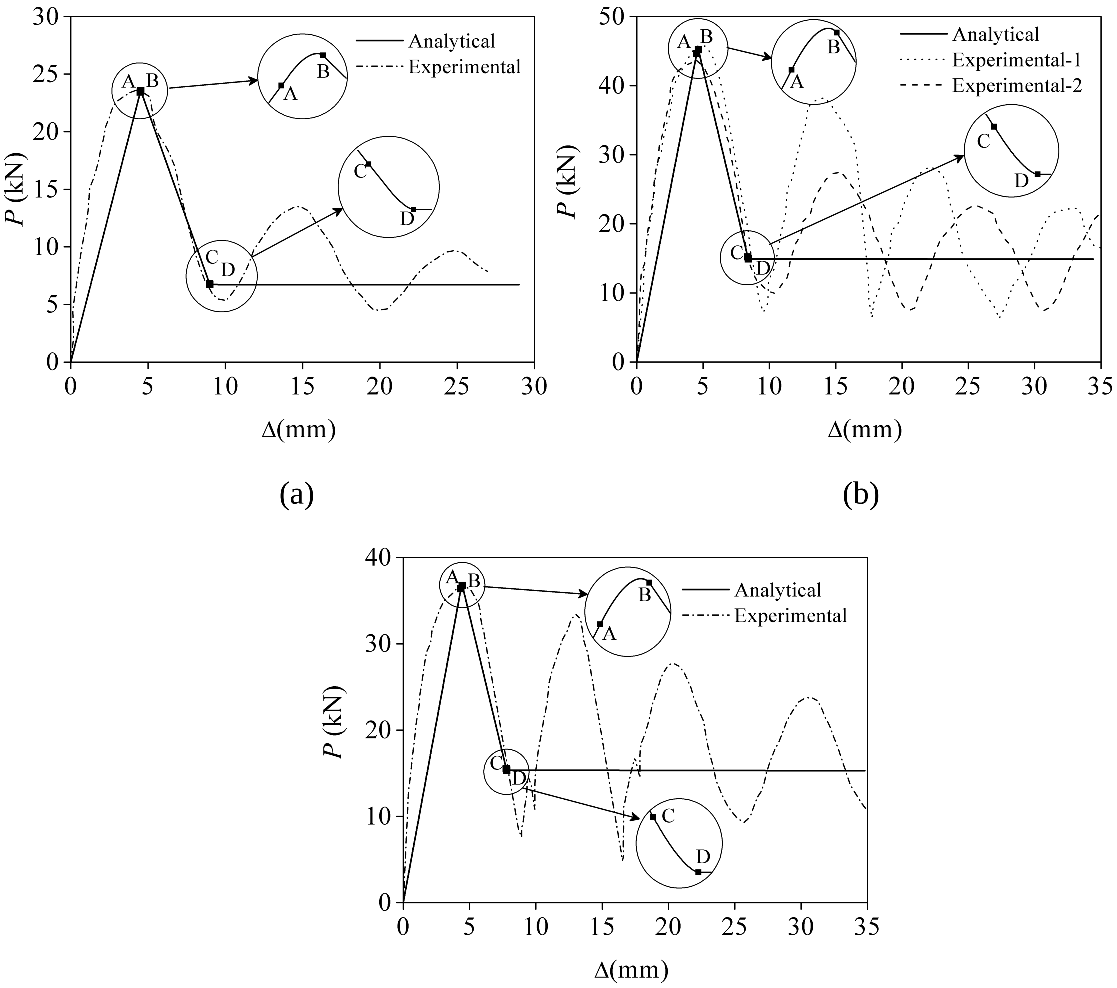

(a) (b)

(c)

Fig. 8. Comparison of load-displacement curve between analytical solution and experimental results for (a) specimen LECM40, (b) specimen LECM80, and (c) specimen LEEM 80.

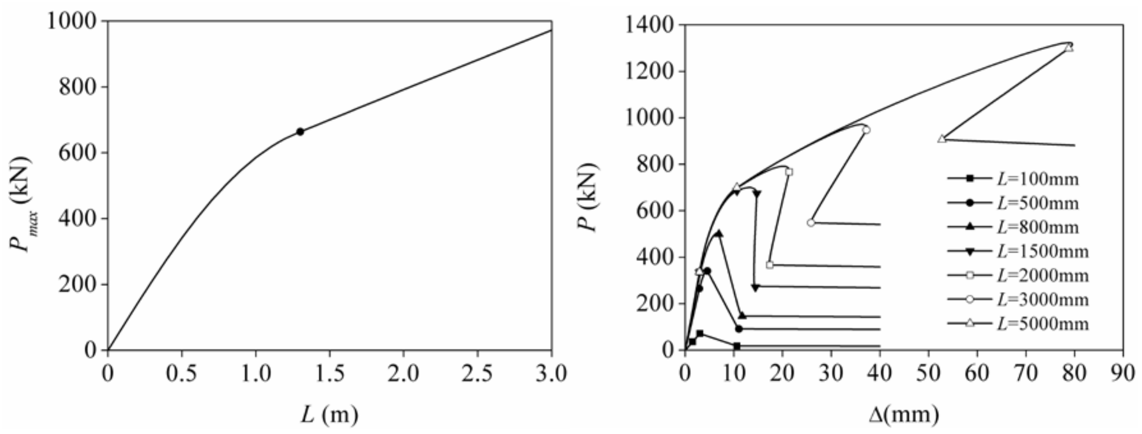

(a) (b)

Fig. 9. Effect of bond length on (a) ultimate load and (b) load-displacement curve.

Table 1 Comparison of ultimate load between analytical solution and experimental results of Rajaie [46].

No.	L (mm)	P_{emax} (kN)	P_{max} (kN)	$(P_{max}-P_{emax})/P_{emax}$ (%)
1	150	43.4	41.8	−3.8
2	200	55.8	55.7	−0.3
3	300	85.2	83.3	−2.2
4	400	115.6	110.8	−4.2
5	500	145.6	137.9	−5.3
6	600	168.6	164.6	−2.4
7	700	187.2	190.9	2.0

Table 2 Comparison of ultimate load between analytical solution and experimental results of Chen et al. [47].

No.	L (mm)	P_{emax} (kN)	P_{max} (kN)	$(P_{max}-P_{emax})/P_{emax}$ (%)
1	320	381.3	385.6	1.1
2	340	432.9	409.5	−5.4
3	360	462.6	433.4	−6.3
4	380	479.1	457.3	−4.6

Table 3 Comparison of ultimate load between analytical solution and experimental results of Zhang et al. [19].

No.	Specimen	E_s (GPa)	L (mm)	τ_u (MPa)	τ_r (MPa)	δ_1 (mm)	δ_2 (mm)	P_{emax} (kN)	P_{max} (kN)	$(P_{max}-P_{emax})/P_{emax}$ (%)
1	FR1+CG1	60.83	100	8.2	2.8	1.31	3.86	19.4	19.0	−2.0
2	FR1+CG2	60.83	100	7.9	2.5	1.05	6.10	18.6	18.5	−0.5
3	FR1+CG3	60.83	100	8.4	3.1	0.72	5.60	19.9	19.6	−1.5
4	FR1+CG4	60.83	100	8.7	2.6	0.66	4.18	20.6	20.2	−1.9
5	FR1+CG4	60.83	200	8.7	2.6	0.66	4.18	26.9	38.8	44.2
6	FR1+CG4	60.83	350	8.7	2.6	0.66	4.18	37.1	56.7	52.8
7	FR2+CG1	43.5	100	12.3	3.3	2.34	7.66	30.9	30.3	−1.9
8	FR2+CG2	43.5	100	7.9	2.4	2.30	6.48	20.0	19.6	−2.0
9	FR2+CG3	43.5	100	12.3	3.3	1.78	7.80	31.0	30.4	−2.0
10	FR2+CG4	43.5	100	13.2	3.8	2.50	6.50	33.3	32.3	−3.0
11	FR2+CG4	43.5	200	13.2	3.8	2.50	6.50	55.6	59.9	7.7
12	FR2+CG4	43.5	350	13.2	3.8	2.50	6.50	67.9	85.9	26.5
13	FR3+CG1	163.33	100	13.1	4.1	3.32	9.60	32.6	32.4	−0.6
14	FR3+CG2	163.33	100	10.6	3.1	2.97	9.95	26.7	26.2	−1.9
15	FR3+CG3	163.33	100	12.4	4.4	2.61	8.70	30.8	30.7	−0.3
16	FR3+CG4	163.33	100	14.4	5.6	2.90	6.40	35.8	35.5	−0.8
17	FR3+CG4	163.33	200	14.4	5.6	2.90	6.40	67.6	69.7	3.1

Table 4 Comparison of ultimate load between analytical solution and experimental results of Zhang and Benmokrane [20].

Specimen	L (mm)	τ_u (MPa)	τ_r (MPa)	δ_1 (mm)	δ_2 (mm)	P_{emax} (kN)	P_{max} (kN)	$(P_{max}-P_{emax})/P_{emax}$ (%)
AREM40	40	14.85	3.93	1.22	3.25	14.00	13.91	−0.64
AREM80	80	10.76	2.84	1.37	4.44	20.30	20.04	−1.28
LECM40	40	23.75	6.78	4.49	8.99	23.60	23.55	−0.21
LECM80	80	22.92	7.52	4.51	8.37	45.50	45.25	−0.55
LEEM40	40	21.54	8.06	4.22	7.89	21.40	21.36	−0.19
LEEM80	80	18.62	7.73	4.34	7.76	37.00	36.80	−0.54

HIGHLIGHTS

(1) Three-dimensional analytical model is proposed for the pullout response of anchors.

(2) The ultimate load and load-displacement response have been predicted and verified.

(3) The bond length determines the possible stages in the evolution of debonding.

(4) The bond length plays a pivotal role in the load-displacement response of anchors.